

Analysis and Reduction of the Near Magnetic Field Emission From Toroidal Inductors

Boyi Zhang, *Student Member, IEEE*, and Shuo Wang , *Fellow, IEEE*

Abstract—The near magnetic field emitted from magnetic components may generate electromagnetic interference (EMI) and degrade EMI filter's performance. This article discussed the near magnetic field emission from toroidal inductors. The emission mechanisms are analyzed for different inductor winding structures with either common-mode (CM) or differential-mode (DM) excitation. The winding structures with low near magnetic field emission are identified. A CM inductor structure is proposed to improve inductor's high-frequency CM performance and greatly reduce its near magnetic field emission due to DM currents. The improvements are achieved with a small extra toroid. The proposed structure can also increase CM inductor's DM inductance for DM noise reduction at the expense of a reduced DM saturation current. To avoid saturation, a design procedure is developed for the proposed CM inductor to achieve desired CM inductance, minimized near magnetic field emission, high DM inductance, and optimal magnetic flux density. Three-dimensional (3-D) finite-element analysis models were developed and experiments were conducted to validate the developed theory and techniques. EMI measurement results show that the proposed CM inductor has a better performance for both DM and CM noise reduction than a conventional CM inductor.

Index Terms—Electromagnetic interference (EMI) filters, inductors, leakage inductance, magnetic components, magnetic flux, near magnetic field, reluctance.

I. INTRODUCTION

In high power density power converter design, power components are very close to each other. This increases the concern of near magnetic field couplings due to magnetic components, as shown in Fig. 1. Some existing literatures have focused on the near magnetic field couplings within electromagnetic interference (EMI) filters. Parasitic parameters' effects are discussed in [1]–[3]. The fact that EMI filter performance is degraded due to the near magnetic field emission from inductors was well recognized and discussed in [1]–[7]. Techniques to improve inductor performance with parasitic capacitance cancellation are developed in [4] and [5]. In addition, the near magnetic field emission in power electronics circuits was studied in [8]–[15]. Circuit models had been developed for the mutual couplings between inductors and other components. The equivalent current loop technique was proposed in [11] to predict

Manuscript received April 27, 2018; revised August 21, 2018, June 11, 2019, and August 24, 2019; accepted November 4, 2019. Date of publication November 14, 2019; date of current version February 20, 2020. This work was supported in part by National Science Foundation under Award 1611048. Recommended for publication by Associate Editor J. A. Cobos. (*Corresponding author: Shuo Wang*.)

The authors are with the University of Florida, Gainesville, FL 32611 USA (e-mail: zby0070@ufl.edu; shuowang@ieee.org).

Color versions of one or more of the figures in this article are available online at <http://ieeexplore.ieee.org>.

Digital Object Identifier 10.1109/TPEL.2019.2953748

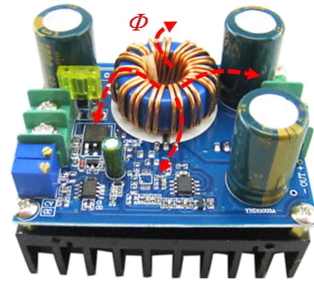


Fig. 1. Near magnetic field generated by an inductor can be detrimental to circuit's normal operation.

and model near magnetic field. An inverse-problem-based resolution technique was adopted in [12] to model the near magnetic field in power electronics circuits.

In a power electronics system, the major sources of near magnetic field emission are magnetic components, such as inductors and transformers [6], [7]. The analysis and experimental results presented in [1]–[7] proved that the near magnetic field emitted from magnetic components may increase EMI and degrade EMI filter's performance. Hariya *et al.* [13] presented that the near magnetic field emitted from a transformer could increase eddy current power loss. Thus, it is important to reduce near magnetic field emitted from magnetic components.

Magnetic shielding [14] is one of the techniques used to reduce near magnetic field emission. However, the use of the magnetic shielding will inevitably increase the volume and cost. Besides, the effectiveness of the magnetic shielding varies for different inductor structures. An experimental comparison is included in Section II-A.

Near magnetic field emission can also be reduced by properly designing inductors. Wang *et al.* [10] focused on the inductor near magnetic field emission at high frequencies. The near magnetic field behavior of inductors can be described with Biot–Savart's Law. However, it is very difficult to use it for complex inductor structures. The near magnetic field behavior of planar transformers and common-mode (CM) inductors was discussed in [6]. A stacked CM inductor structure and its model were proposed in [6] to address the near magnetic field emission issues. But the magnetic flux analysis presented in [6] cannot fully explain the uneven magnetic field distribution. Simulations and experiments were conducted in [15] to investigate the near magnetic field emission from inductors based on various winding structures. But it lacks theoretical analysis.

For filter inductor design, existing research has been focused on the reduction of inductor size and increasing of CM inductor's differential-mode (DM) inductance. In [16] and [17], integrated CM and DM inductors were proposed to achieve the goal, but the near magnetic field emission is not investigated.

TABLE I
COMPARISON OF CONVENTIONAL TOROIDAL INDUCTOR AND COMMERCIAL SHIELDED INDUCTORS

Structure	Prototypes	Inductance	Near Magnetic Field Emission at 10 kHz	Maximum Near Magnetic Flux Density at 10 kHz (μT)	Volume (mm^3)	Unit Price (USD)	Saturation current (A)	Design Flexibility
Regular Toroidal Inductor		21 μH		14.8	4517.0	\$ 0.72	20	High
Regular Fully Shielded Inductor		22 μH		11.7	6514.2	\$ 4.71	14	Low
Regular Partially Shielded Inductor		20.7 μH		37.1	5171.12	\$ 2.03	9.8	Low

Different from these existing techniques, this article will focus on the near magnetic field emission behavior of both DM and CM inductors. Techniques to analyze and reduce the near magnetic field emission with different winding structures are developed. A new CM inductor structure with smaller near field emission and larger leakage inductance, which is good to attenuate DM noise than conventional CM inductors is proposed. A design procedure is developed for the proposed inductor structure to achieve desired CM inductance, reduced near magnetic field, increased DM inductance, and unsaturated core. Both three-dimensional (3-D) finite-element analysis simulations and experiments were conducted to validate the developed theory and techniques.

II. NEAR MAGNETIC FIELD ANALYSIS FOR DM AND CM INDUCTORS

Inductors are one of the most important passive components in power electronics systems. They can be used as energy storage devices in power converters/inverters to achieve energy conversion functions. It can also be used as filter components to reduce EMI generated by power electronics systems.

Inductor winding structures can be categorized as single-ended structure and balanced structure. For single-ended structure, there is only one winding on the core. For balanced winding structure, there are two, three, or more identical windings on the core. This article will focus on single-winding and two-winding inductors. Based on the current directions in the windings, the inductors can be categorized as DM and CM inductors. The CM current CM_I in the two windings of a two-winding CM inductor has the same direction and magnitude. The DM current DM_I in the two windings of a two-winding DM inductor has the same amplitude but with inverse directions. In this article, it is assumed that the winding turns are evenly distributed around the cores. The developed theory and techniques in this article can be extended to three-winding or multiwinding inductors.

A. Comparison of Magnetic Emission of Regular Toroidal Inductors and Existing Shielded Inductors

There are commercial shielded inductors available in the market. A comparison of a conventional toroidal inductor and two commercial shielded inductors is conducted in Table I. All of them are one-winding inductors with similar inductance. Due to

the availability, their saturation currents are different. This does not influence the comparison of the measured near magnetic field in Table I as these inductors are tested with an identical current that is smaller than their saturation currents.

A 10-kHz, 5 A current was added to each inductor. The near magnetic field was measured on a plane 20 mm above the inductors. The measurement setup detail will be addressed in Section V. The measured near magnetic flux distribution and the highest flux density are compared in Table I. As shown in the table, compared with the regular toroidal inductor, the fully shielded inductor can reduce near magnetic field emission by 20% at cost of larger volume, higher expense, and smaller saturation current. The partially shielded inductor has higher volume and expense but higher near magnetic field intensity, because of the leakage flux from the exposed winding on the two core openings, than the conventional toroidal inductor. The conventional toroidal inductor has smaller near magnetic field emission than the partially shielded inductor because the leakage magnetic field of its winding turns is partially canceled due to the round core shape. The detailed analysis about this will be presented in Section II-B.

Furthermore, the conventional toroidal inductor has more flexibility in the design at much lower cost than commercial shielded inductors which must be customized, and their inductance values are fixed.

Because of the reasons mentioned above, it is necessary to investigate the near magnetic field emission and its reduction for conventional toroidal inductors.

B. Near Magnetic Field Emission Analysis for DM Inductors

The near magnetic field emitted from inductors to the space can couple to other components or circuits nearby. It could compromise the normal operation of the power converter and the EMI reduction measures used in the converter. Since the distance between the inductor and these components or circuits is smaller than 1/20 of the wavelength of the electromagnetic waves (<30 MHz is investigated here) emitted from the inductor, the near magnetic field should be investigated. Fig. 2 shows two conventional inductor structures: a single-ended one-winding structure with two terminals and a balanced two-winding structure with four terminals. They can carry either DM current I_{DM} or CM current I_{CM} , as shown in Fig. 2.

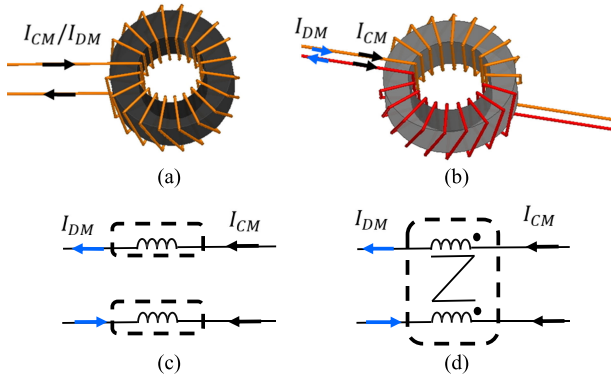


Fig. 2. Conventional inductor structures. (a) Single-ended one-winding inductor. (b) Balanced two-winding CM inductor. (c) Two single-ended one-winding inductors used in a circuit conducting either CM or DM current. (d) One balanced two-winding CM inductor used in a circuit conducting either CM or DM current.

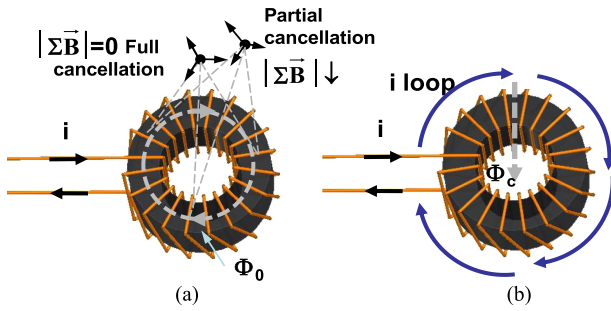


Fig. 3. Near magnetic field of a single-ended inductor. (a) Directly generated by the winding turns. (b) Generated by the equivalent current loop.

Factors such as core saturation, desired inductance, and power loss should be considered in inductor design. In many power electronics applications, because the DM current includes not only DM noise current but also power current so it is much higher than the CM current. As a result, the core permeability of DM inductors is usually smaller than that of CM inductors to avoid saturation. If the inductance of one single-ended one-winding inductor is L , then when two single-ended inductors are used on two power delivery paths separately in Fig. 2(c), the CM inductance will be $L/2$ and the DM inductance will be $2L$. Fig. 3(a) shows the analysis of the near magnetic field emission for this single-ended one-winding inductor. Two major near magnetic field mechanisms are identified for the inductor: the magnetic flux Φ_0 directly generated by the winding turns and the magnetic flux Φ_C generated by the equivalent current loop along the toroidal core, as shown in Fig. 3(a) and (b), respectively.

In Fig. 3(a), most of Φ_0 is confined within the magnetic core due to its high permeability. There is a very small portion of Φ_0 emitted to the air. This small portion tends to cancel itself as the vector sum of the B field generated by each winding turn tends to cancel each other in the space, as shown in Fig. 3(a). This cancellation is due to the fact that the winding turns are evenly distributed along the toroidal core in 360° . The detailed proof can be found in the Appendix in which a partial element equivalent circuit (PEEC) method is used to calculate the near magnetic field outside the toroidal core inductor.

On the other hand, the equivalent current loop caused by the winding along the toroidal core will generate flux Φ_C emitting

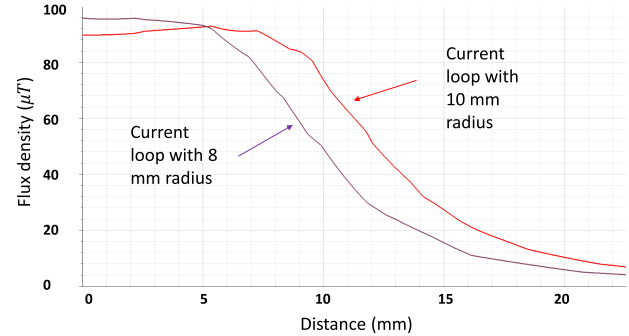


Fig. 4. Flux density comparison between two current loops with radius 8 and 10 mm.

to the space. It has been proven that the magnetic flux density of a circular current loop reaches the highest at the center line of the circle [20]. The flux linkage Φ_C generated from the current loop with current i is given as follows:

$$\Phi_C = i \left(\mu_0 r \left[\ln \left(\frac{1.05r}{a} \right) \right] \right) \quad (1)$$

where r is the average radius of the circular current loop, and a is the radius of the winding conductor. Based on the analysis mentioned above, flux Φ_C should be dominant in the emitted near magnetic field of this inductor. Based on (1), the inductor with smaller average radius has smaller Φ_C and, therefore, smaller near magnetic field emission. Fig. 4 shows the simulated flux density (y-axis) of two equivalent current loops with 8 and 10 mm radii carrying identical currents as a function of the distance (x-axis) to the center line of the current loops.

In this article, all the simulations are conducted in Ansys Maxwell. First, 3-D physical models are drawn based on the dimensions of real magnetic cores and winding wires. A material is then assigned to each solid entity. The properties of the material include its permeability, conductivity, mass, conductivity, etc. The solver is magnetostatics. Current excitations are added to the wire terminals as needed. The simulation region is set to be much larger than the dimensions of the inductors, so that the boundaries will have small influence to simulation results. After a simulation is done, the magnetic field distribution can be investigated.

Although 2-D simulations can also be conducted for the inductors, 3-D simulations can show flux density magnitude and directions on different heights and planes, which is very difficult to show in 2-D simulations. Three-dimensional simulations are also better than 2-D simulations to show the near magnetic flux distribution around the components. Because of this, 3-D simulations are employed in this article. The flux density is recorded on a plane 5 mm above the inductors.

It is shown in Fig. 4 that the current loop with bigger radius generates higher magnetic flux density than the one with smaller radius except at the locations close to the center line of the current loops. This agrees with (1). Fig. 5 shows the simulated near magnetic field distribution in Ansys Maxwell 3D. In the simulations, the core has a relative permeability of 60. It has an inner diameter of 15 mm, outer diameter of 25 mm, and a height of 10 mm. The number of winding turns is 20, and the wire is AWG #24 (0.51 mm diameter). DC current of 2 A is added. The color map scales of Fig. 5(a) and (b) are the same. As shown in Fig. 5, the near magnetic field generated by the equivalent current

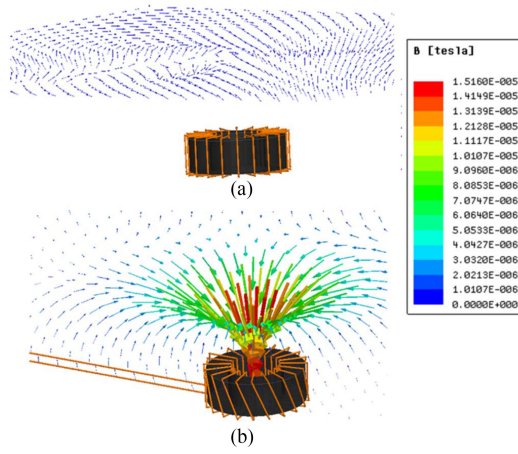


Fig. 5. Simulated near magnetic field of a single-ended one-winding inductor generated by (a) winding turns and (b) equivalent current loop.

loop has much higher magnetic flux density than that generated by the winding turns. The Φ_C below the bottom of the inductor is not shown in Fig. 5(b), but its distribution is similar to that on the top but with reverse direction. Because Φ_C is dominant, using a toroidal inductor with small average radius can reduce the emitted near magnetic field for this inductor winding structure [20]. It validated the analysis mentioned above.

From (A17)–(A28) in the Appendix and (1), it can be concluded that although it is possible to calculate near magnetic field outside the inductor, the process is very complicated and time-consuming, especially for more complex structures. Thus, reluctance models are developed for convenient analysis in the rest of the article.

C. Near Magetic Field Emission Analysis for CM Inductors

The balanced two-winding CM inductor in Fig. 2(b) is usually used in EMI filters to attenuate both CM and DM noises. If the inductance of each winding is L , then when it is used to attenuate both CM and DM noises as in Fig. 2(d), the total CM inductance is close to L and the DM inductance is the leakage inductance of the two windings. More specifically, the two windings are directly coupled for CM currents but inversely coupled for DM currents. The inductor usually has a core with high permeability, and the magnetic field generated by the CM currents in two windings enhance inside the core so it has high CM impedance to attenuate CM noise. When it carries CM currents, the near magnetic field generated by winding turns outside of the inductor is very small due to the same reason, as shown in Fig. 3(a). Fig. 6(a) shows the near magnetic field generated by two equivalent current paths. Φ_a is the near magnetic field generated by the top path, and Φ_b is the near magnetic field generated by the bottom path. Most of the near magnetic field is canceled between the two current paths, and the near magnetic field is enhanced on the two sides of the two current paths because the near magnetic field generated by the two current paths has the same direction on the two sides. The near magnetic field is also determined by the returning current paths, which are related to the circuit layout. The returning current paths could be on a ground plane. In summary, the near magnetic field is generated by the two equivalent current paths and their returning paths, as shown in Fig. 6(a). If the circuit layout can be properly designed to minimize the loop areas between the two current

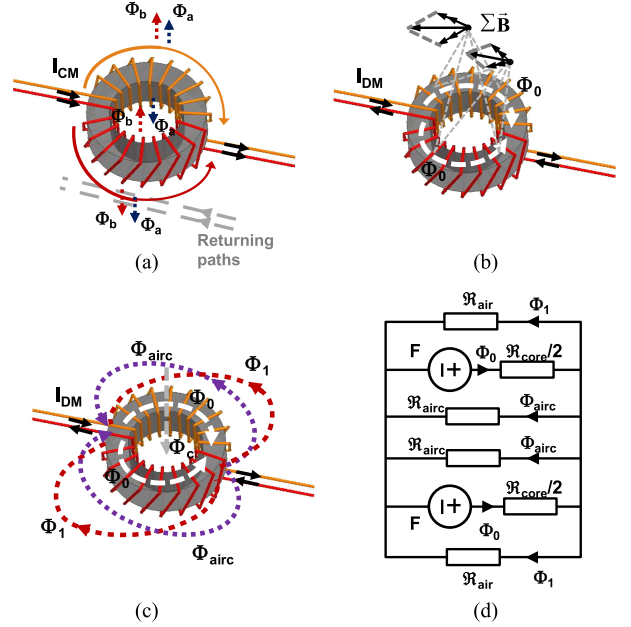


Fig. 6. Near magnetic field of a balanced two-winding CM inductor. (a) Excited with CM current. (b) Excited with DM currents. (c) Near magnetic field due to DM currents. (d) Magnetic reluctance model with DM excitations.

paths and the returning current paths, the near magnetic field can be minimized.

On the other hand, the leakage inductance of the two windings is usually used as the DM inductance to attenuate DM noise. When the inductor carries DM currents, the magnetic field generated by the two windings mostly cancels inside the core, so most of the magnetic field generated by the DM currents is emitted to the air. Fig. 6(b) shows that the magnitude of the vector sum of the B field generated by two windings is bigger than the magnitude of the vector of the B field generated by a single winding in the space. This is due to the fact that the two windings carry inverse DM currents, and each is evenly distributed along the toroidal core across 180°. Because of this, the emitted near magnetic field due to DM currents is much stronger than that due to CM currents when the DM and CM currents have the same magnitude.

Fig. 6(c) and (d) shows the near magnetic field emission due to DM currents and the magnetic reluctance model for a balanced two-winding inductor when it carries DM currents in its two windings.

In Fig. 6(c), the magnetic flux flowing within the core is Φ_0 . The magnetic flux flowing on the top and bottom sides of the core within the air between the two winding openings is Φ_{airC} . The magnetic flux flowing on the front and back sides of the core within the air between the two winding openings is Φ_1 .

In the magnetic reluctance model shown in Fig. 6(d), R_{air} and R_{airC} are the equivalent reluctances of the air on the front or back side and on the top or bottom side. R_{core} is the equivalent reluctance of the magnetic core. F is the magnetomotive force (MMF), which is equal to the number N of winding turn times current I , generated by each winding. The reluctances meet the following condition:

$$\frac{R_{core}}{2} \ll \frac{R_{air}}{2}, \frac{R_{airC}}{2}. \quad (2)$$

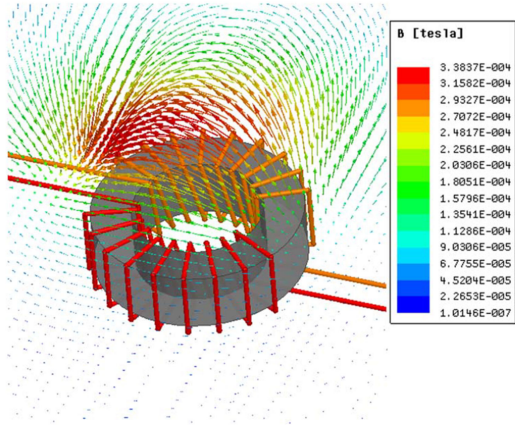


Fig. 7. Simulated near magnetic field of a balanced two-winding inductor with a DM current excitation.

The Φ_0 can be solved as follows:

$$\Phi_0 = \frac{\left[\frac{R_{\text{core}}}{2} - \left(\frac{R_{\text{core}}}{2} // \frac{R_{\text{air}}}{2} // \frac{R_{\text{air}C}}{2} \right) \right] F}{\left[\frac{R_{\text{core}}}{2} // \frac{R_{\text{air}}}{2} // \frac{R_{\text{air}C}}{2} + \frac{R_{\text{core}}}{2} \right] \cdot \frac{R_{\text{core}}}{2}}. \quad (3)$$

In (3), the Φ_0 is very small because the numerator is very small due to the fact that R_{air} and $R_{\text{air}C}$ are much bigger than R_{core} . The magnetic field generated by the two windings mostly cancels out.

The Φ_1 and $\Phi_{\text{air}C}$ can be solved as follows:

$$2(\Phi_1 + \Phi_{\text{air}C}) \approx 2F \left(\frac{1}{R_{\text{air}}} + \frac{1}{R_{\text{air}C}} \right). \quad (4)$$

In (4), $2(\Phi_1 + \Phi_{\text{air}C})$ represents the total emitted near magnetic flux, which is twice of the emitted magnetic flux of single winding. Φ_1 is determined by F/R_{air} and, $\Phi_{\text{air}C}$ is determined by $F/R_{\text{air}C}$.

In Fig. 6(c), Φ_C is generated by the equivalent DM current loop similar to that in Fig. 3(b). It is much smaller than $2(\Phi_1 + \Phi_{\text{air}C})$ due to the fact that the DM current loop has only one turn, but $2(\Phi_1 + \Phi_{\text{air}C})$ represents almost all the magnetic flux of the DM inductance. Furthermore, the magnetic flux Φ_0 inside the core is very small, as shown in (3). Because of these, the magnetic flux of the leakage (DM) inductance of the CM inductor is mostly determined by $2(\Phi_1 + \Phi_{\text{air}C})$. Because $2(\Phi_1 + \Phi_{\text{air}C})$ is generated by DM current I_{DM} , the DM inductance L_{DM} of the CM inductor is, therefore, given as

$$L_{\text{DM}} = \frac{2(\Phi_1 + \Phi_{\text{air}C})}{I_{\text{DM}}}. \quad (5)$$

Fig. 7 shows the simulated near magnetic field of a CM inductor excited with DM currents. In the simulations, the core has a relative permeability of 5000. It has an inner diameter of 13.7 mm, outer diameter of 22.1 mm, and a height of 6.35 mm. The number of turns is ten for each winding, and the wire is AWG #24 (0.51 mm diameter). DM current of 2 A is added.

Based on the flux direction shown in Fig. 7, it is shown that the $2(\Phi_1 + \Phi_{\text{air}C})$ is the major part of near magnetic field emission for this winding structure. It is much higher than Φ_C .

When inductors are used in EMI filters to reduce EMI and meet EMI standards, the magnitudes of the noise currents inside the inductors vary depending on filter topology. For example, if the filter is a two-stage filter that uses two inductors, then

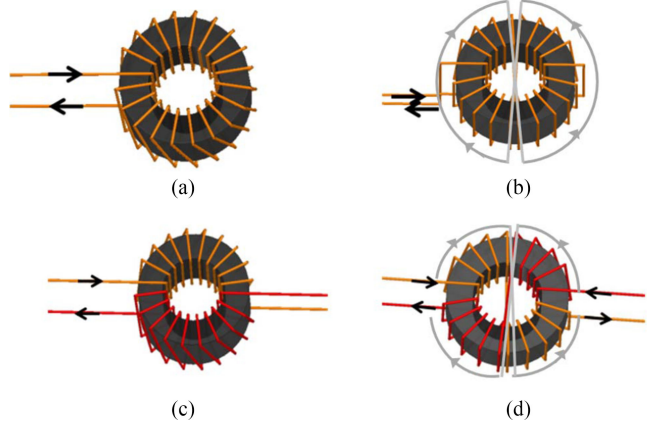


Fig. 8. DM inductors with winding structures (a), (b), (c), and (d).

the first stage has a much higher noise current than the second stage; so even the EMI current at the output of the second stage is reduced to meet EMI standards, the EMI current in the inductor of the first stage may still be large. Also, even the near magnetic field generated from the CM current in a CM inductor is small as proved above, the near magnetic field due to the leakage inductance of the CM inductor when the inductor is excited with DM currents could be significant. This is because the DM inductance is the leakage inductance of the CM inductor, almost all of the magnetic field generated by the DM current was emitted to the space, so it is not negligible. Furthermore, even if the EMI current is small, the near magnetic field generated from the current may still be critical to EMI filter performance. This is because even a very small near magnetic coupling can cause detrimental effects to EMI filter performance, as proved in [1] and [3]. As an example, the very small coupling between the filter inductor and capacitors can greatly degrade EMI filter high-frequency performance due to the fact that the noise currents in the filter inductor and the capacitors are significantly different. As a rule of a thumb, if the current magnitudes in an inductor and another filter component are significantly different, a very small inductive coupling due to the emitted near magnetic field from the inductor may significantly degrade the EMI filter high-frequency performance.

III. WINDING STRUCTURES THAT CAN REDUCE NEAR MAGNETIC FIELD EMISSION

The main sources of near magnetic field emission in DM inductors and CM inductors are identified in Section II. In this section, several winding structures that can reduce the near magnetic field emission of DM or CM inductors will be analyzed.

A. Winding Structures for DM Inductors

Fig. 8 shows four winding structures for DM inductors. Structure (a) is the same as the single-ended one winding structure in Fig. 2(a). Its near magnetic field distribution has been analyzed in Section II. Structure (b) is still a single-ended structure but has a winding cross at the $\frac{1}{4}$ and $\frac{3}{4}$ of the winding length around the core. As a result, there are two equivalent current loops: one has an inverse current direction to the other, as shown by the arrow line in Fig. 8(b). Structure (c) is a balanced two-winding structure with two windings directly coupled for DM currents. From the magnetic field point of view, it is the same as the winding structure (a). Structure (d) is also a balanced

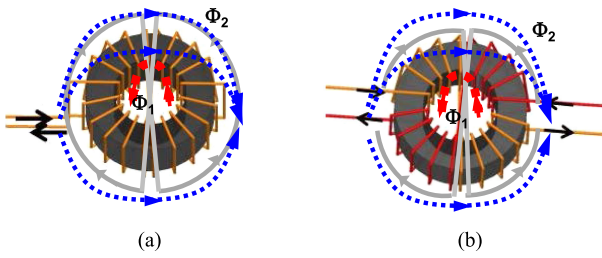


Fig. 9. Near magnetic field distributions of DM inductor winding structure (b) and (d).

two-winding structure with two windings directly coupled for DM currents. However, it has a winding cross in the middle of each winding; as a result, it has a similar equivalent current loop to that in structure (b). In contrast to the positions of the two input terminals, the two output terminals switched positions, shown in Fig. 8(d).

Because structure (a) has been analyzed in Fig. 2(a) and structure (c) has a similar near magnetic field distribution to that in Fig. 2(a), they will not be analyzed here. It has been analyzed in Fig. 3(a) that the B field generated by each winding turn tends to cancel each other in the space so that the emitted near magnetic flux is small. On the other hand, the Φ_C generated by the equivalent current loop is dominant in the near magnetic field. For structures (b) and (d), the equivalent current loop is twisted in the center, so there are two small current loops with reversed current directions. The magnetic fluxes generated by these two loops have inverse directions but with the same magnitude so their magnetic field distributions are more complicated than the other two structures.

In Fig. 9, because the two twisted equivalent current loops carry inverse currents with the same magnitude, they generate inverse magnetic field with the same magnitude. The magnetic fields generated by these two current loops tend to cancel each other in the space. Because of this, the near magnetic field emission is smaller than that of structures (a) and (c). For the space close to the center of the inductor, as shown in Fig. 9, the inner magnetic flux Φ_1 flows through a flux loop linking the two equivalent current loops, and it has an inverse direction to the outer magnetic flux Φ_2 , which flows through a flux loop linking the two equivalent current loops from the outside. This is due to the fact that the magnetic flux generated by a current loop always flows along flux loops from the inside to the outside of the current loop. Only the top half of the magnetic flux loops is shown in Fig. 9. The bottom half is the same as the top half except the flux direction is reversed. As analyzed above, inductors (b) and (d) should have a similar near magnetic field distribution, as shown in Fig. 9.

Fig. 10 shows the simulated near magnetic field for structures (b) and (d). The simulation condition is the same as used in Fig. 5. The color map scales of the two figures are the same. Only the magnetic flux of the outer loop is shown in the figure as the observing plane is above the inner magnetic flux loop. The results verified the analysis.

B. Winding Structures for CM Inductors

Fig. 11 shows three winding structures for CM inductors. Inductor winding structure (e) is a regular CM inductor. Each winding of the inductor winding structure (f) is split to two winding halves. The four winding halves have a cross in the

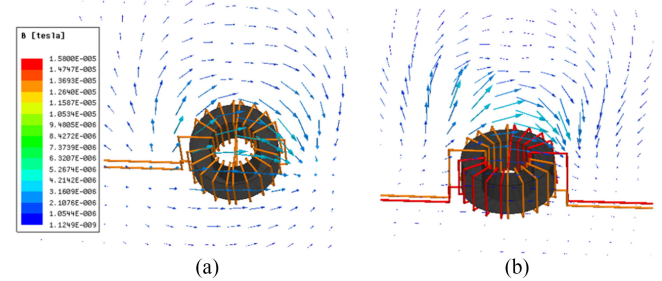


Fig. 10. Simulated magnetic fields for inductor winding structure (b) and (d).

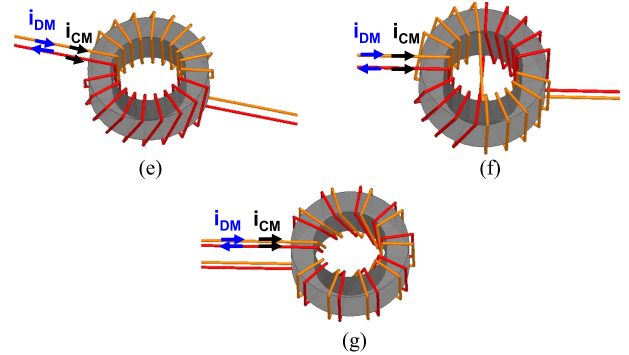


Fig. 11. CM inductors with winding structure (e), (f), and (g).

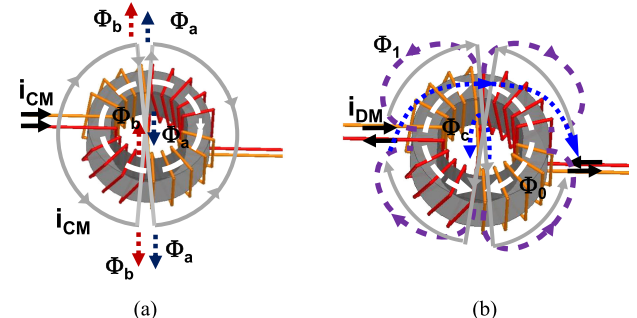


Fig. 12. Near magnetic field of inductor winding structure (f). (a) With CM currents. (b) With DM currents.

middle of the core, as shown in Fig. 11(f). The two windings of the inductor winding structure (g) are bifilar. Because the leakage inductance of CM inductors is usually used for DM noise reduction, all of three inductor winding structures will be analyzed under both CM and DM current excitations.

The near magnetic field emission of the inductor winding structure (e) under DM or CM current excitations has been analyzed in Fig. 6.

For the inductor winding structure (f), it has four winding halves along the core, and each has a 90° span on the core. Because all winding turns are equivalently same as those of a regular CM inductor, when the two windings conduct CM currents, the near magnetic field generated by winding turns is similar to that in Fig. 3(a). The near magnetic field generated by equivalent current loops is shown in Fig. 12(a), which is similar to that in Fig. 6(a), as the near magnetic fields generated by two cross segments are mostly canceled since they carry inverse currents. As discussed previously, the near magnetic field is also related to current returning paths.

When the two windings conduct DM currents, the near magnetic field generated by winding turns can still be analyzed

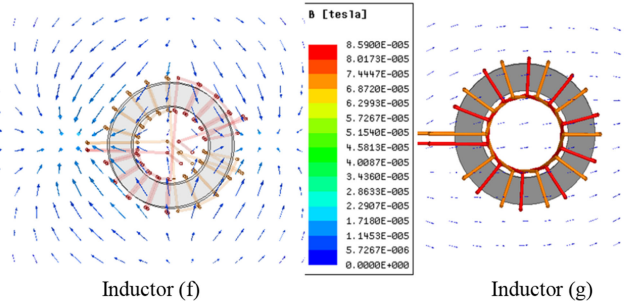


Fig. 13. Simulated near magnetic field of inductor (f) and (g) with DM currents.

similarly to those in Fig. 6(b)–(d). The difference is each winding spans 90° instead of 180° , as a result the leakage flux generated by these four winding halves also spans 90° , as shown by Φ_1 in Fig. 12(b). Because four winding halves are interleaved along the core, the coupling between the two windings is higher than that of the conventional inductor winding structure (e). So the emitted near magnetic field, which is due to leakage inductance of two windings, is smaller than that of the structure (e). As a result, its leakage (DM) inductance is also smaller than conventional winding structure (e). Because of this, winding structure (f) sacrifices DM inductance to reduce near magnetic field emission. It is therefore preferred when a reduced near magnetic field is desired, and the reduced DM inductance is still acceptable.

There are two equivalent reverse current loops in this winding structure, as shown in Fig. 12(b). Similar to winding structure (d) with DM current excitation, the near magnetic field generated by these two equivalent current loops can be represented similarly to the magnetic field distribution of the inductor winding structure (d) in Fig. 9. It is shown as the blue dash lines in Fig. 12(b). For the same reason as for Fig. 6(b)–(d), compared with the near magnetic field generated by winding turns, it is very small, so it can be ignored.

The inductor winding structure (g) has the smallest near magnetic field emission with DM current excitations. This is because the magnetic field generated by the two bifilar windings cancels each other as the two windings have the almost same position and with the same magnitude but inverse current. The near magnetic field emission due to CM currents is mostly canceled, as analyzed in Fig. 3(a). Because of this, both the near magnetic field emissions from DM and CM currents are small. The disadvantage of this structure is the leakage (DM) inductance that is very small, so it mostly cannot be used to attenuate DM noise.

Simulation results for inductor structures (f) and (g) with DM excitations are shown in Fig. 13 under the same condition as used in Fig. 7. The near magnetic flux spans 90° for structure (f), as analyzed above. Structure (g) has a much smaller near magnetic field emission than structure (f). They validated the analysis mentioned above.

IV. PROPOSED CM INDUCTOR WINDING STRUCTURE TO REDUCE NEAR MAGNETIC FIELD EMISSION WITH INCREASED DM INDUCTANCE

Although winding structures (f) and (g) can reduce the near magnetic field emission, the DM inductance, especially structure (g), is greatly reduced which is not desirable. In this section, a new CM inductor structure that can greatly reduce near magnetic

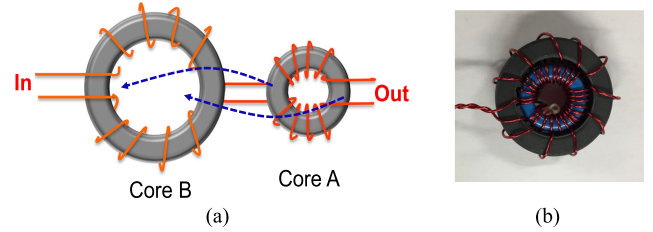


Fig. 14. Proposed CM inductor. (a) Winding connection. (b) Prototype.

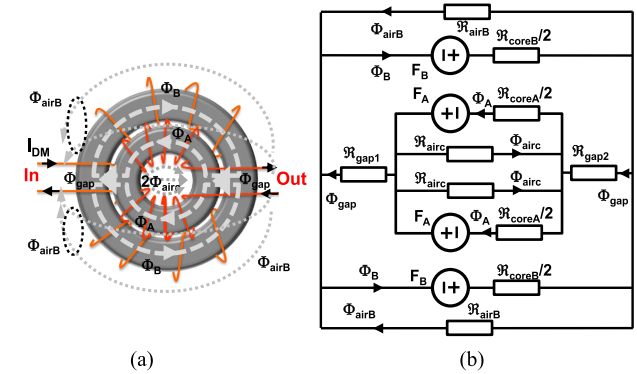


Fig. 15. Proposed CM inductor. (a) inductor picture and magnetic flux with DM excitations. (b) Magnetic circuit.

field emission and increase DM inductance will be presented, and the working principle is to be analyzed.

The proposed CM inductor consists of two cores, core A and core B, as shown in Fig. 14. Core A is smaller than core B and is positioned inside the core B. The winding connections between these two cores are shown in Fig. 14(a). A prototype is shown in Fig. 14(b). In an actual commercial product, a spacer should be placed in the middle of core A between two windings for safety clearance purpose.

The top view of the proposed CM inductor and the equivalent magnetic circuit with DM current excitations are shown in Fig. 15. Similar to other inductors analyzed in previous sections, the near magnetic field emission of the proposed CM inductors with CM current excitation is much smaller than that with DM excitations, so only DM current excitation will be analyzed below.

In Fig. 15, it is assumed that the inductor structure is fully symmetric to a horizontal center line, so all the reluctances and magnetic fluxes in top and bottom parts are equal. R_{coreA} and R_{coreB} represent the magnetic reluctances of core A and core B, respectively. Φ_A and Φ_B represent the magnetic fluxes flowing through R_{coreA} and R_{coreB} , respectively. R_{airC} represents the reluctance of the air across the two winding openings on core A. Φ_{airC} represents the magnetic fluxes flowing through R_{airC} . It is part of the near magnetic field emission of the inductor. R_{airB} represents the magnetic reluctance of the air between two winding openings on core B in Fig. 15(a). Φ_{airB} represents the magnetic fluxes flowing through R_{airB} . It is part of the near magnetic field emission of the inductor. $2\Phi_{airB}$ and $2\Phi_{airC}$ represent all the near magnetic field emitted from the proposed CM inductor with DM current excitations. R_{gap1} and R_{gap2} represent the equivalent magnetic reluctances of the air gaps between core A and core B on each side. Φ_{gap} represents the magnetic flux flowing through R_{gap1} and R_{gap2} . $F_A = I_{DM}N_A$ and $F_B = I_{DM}N_B$ represent the MMF generated by one winding

due to I_{DM} on core A and core B, respectively, whereas N_A and N_B are the numbers of turns of one winding on core A and B, respectively.

A. Near Magnetic Field Emission Reduction

Because $2\Phi_{airB}$ and $2\Phi_{airC}$ represent the near magnetic field emitted from the proposed CM inductor with DM current excitations, and if $2\Phi_{airB}$ and $2\Phi_{airC}$ are greatly reduced, then the near magnetic emission is greatly reduced.

The reluctances meet the following condition:

$$\frac{R_{coreA}}{2}, \frac{R_{coreB}}{2} < R_{gap1}, R_{gap2} \ll R_{airB}, R_{airC}. \quad (6)$$

If $R_{gap} = R_{gap1} + R_{gap2}$, then based on Fig. 15(b), $2\Phi_{airB}$ is given as follows:

$$2\Phi_{airB} \approx \frac{F_B \left(\frac{R_{coreA}}{4} + R_{gap} \right) - F_A \frac{R_{coreB}}{4}}{\left(\frac{R_{coreA}}{4} + R_{gap} + \frac{R_{coreB}}{4} \right) \frac{R_{airB}}{2}} \quad (7)$$

and $2\Phi_{airC}$ is given as follows:

$$2\Phi_{airC} \approx \frac{F_A \left(\frac{R_{coreB}}{4} + R_{gap} \right) - F_B \frac{R_{coreA}}{4}}{\left(\frac{R_{coreA}}{4} + R_{gap} + \frac{R_{coreB}}{4} \right) \frac{R_{airC}}{2}}. \quad (8)$$

From (7), near magnetic field emission $2\Phi_{airB}$ can be eliminated when the following condition is met

$$\frac{F_B}{F_A} = \frac{N_B}{N_A} = \frac{R_{coreB}}{4} / \left(\frac{R_{coreA}}{4} + R_{gap} \right). \quad (9)$$

Condition (9) indicates that F_B should be smaller than F_A due to high reluctance of the air gap. It means smaller number of turns should be used on core B than core A. As shown in Fig. 15(a), $2\Phi_{airB}$ is very important as it represents the near magnetic field emitted around the whole inductor.

From (8), near magnetic field emission $2\Phi_{airC}$ can be eliminated when the following condition is met:

$$\frac{F_B}{F_A} = \frac{N_B}{N_A} = \left(\frac{R_{coreB}}{4} + R_{gap} \right) / \frac{R_{coreA}}{4}. \quad (10)$$

Condition (10) indicates that F_A should be smaller than F_B . It means smaller number of turns should be used for core A than core B. It is a contradict condition to (9); however, as shown in Fig. 15(a), $2\Phi_{airC}$ represents the near magnetic field emitted across the core A. From EMI point of view, if there are no components or sensitive circuits close to the center of core A, $2\Phi_{airC}$ is considered unimportant.

As shown in Fig. 15(a), $2\Phi_{airB}$ and $2\Phi_{airC}$ also partially cancel each other around the horizontal center line close to core A because they have inverse directions.

Based on the analysis mentioned above, condition (9) should be approximately met to reduce near magnetic field emission $2\Phi_{airB}$. The remained near magnetic field can be further reduced by $2\Phi_{airC}$ as analyzed above.

The near magnetic field $2\Phi_{airB}$ of the proposed CM inductor is much smaller than the near magnetic field $2\Phi_1$ of a conventional CM inductor in Fig. 11(e) because 1) the near magnetic field generated by F_A cancels that generated by F_B based on (7) and condition (9); and b) $2\Phi_{airB}$ and $2\Phi_{airC}$ partially cancel each other in the space.

TABLE II
INDUCTOR PARAMETERS FOR EXPERIMENTS AND SIMULATIONS

Proto-types	Core	Outer Diameter	Inner Diameter	Height	Number of turns ¹	μ_r
Regular	B	22.1 mm	13.7 mm	6.35 mm	15	4300
Base-line	A/B	16 mm	9.6 mm	6.3 mm	14	4300
		29 mm	19 mm	7.5 mm		40
Proposed	A	16 mm	9.6 mm	6.3 mm	14	4300
	B	29 mm	19 mm	7.5 mm	5	40

¹The number of turns is the total number of turns on each single winding.

From (6)–(10), R_{coreA} , R_{coreB} , and R_{gap} are given by (11)–(14), respectively

$$R_{coreA} = \frac{l_A}{\mu_A \mu_0 A_A} \quad (11)$$

$$R_{coreB} = \frac{l_B}{\mu_B \mu_0 A_B} \quad (12)$$

$$R_{gap} = \frac{l_{gap1}}{\mu_0 A_{gap1}} + \frac{l_{gap2}}{\mu_0 A_{gap2}} \approx \frac{D_{IB} - D_{OA}}{\mu_0 A_{gap}} \quad (13)$$

$$A_{gap} \approx \frac{\pi (D_{OA} + D_{IB}) (H_A + H_B)}{16}. \quad (14)$$

In the equations, l_A and l_B are the average lengths of core A and B, respectively. A_A and A_B are the cross-sectional area of core A and B, respectively. μ_A and μ_B are the relative permeability of core A and B, respectively. μ_0 is the permeability of air. l_{gap1} and l_{gap2} are the average lengths of air gap 1 and 2, respectively. It is assumed that the two cores are concentric so the airgap length around the circle is constant. A_{gap1} and A_{gap2} are the average cross-sectional area of air gap 1 and 2, respectively, and they are equal to A_{gap} . D_{OA} and D_{IB} are the outer diameter of core A and the inner diameter of core B, respectively. H_A and H_B are the height of the two cores. In (14), the average cross-sectional area of air gap A_{gap} is approximately equal to the $\frac{1}{4}$ cross-sectional area of the whole air gap between the two cores because the magnetic flux across the air gap is zero at the locations of $\frac{1}{2}$ windings and reaches the maximum on the two side openings. It is assumed that D_{OA} and D_{IB} are not very different, and also H_A and H_B are not very different, so the magnetic flux fringing effect is ignored while calculating the reluctance above.

Core dimensions presented in Table II are used in both simulations and experiments to validate the proposed technique. The CM inductors were designed according to the design guidelines presented in Section IV-C, where detailed design procedure will be discussed to achieve desired CM inductance, near magnetic field cancellation, and unsaturated core.

The 3-D models of the CM inductors presented in Table II were developed in Ansys Maxwell 3D. The regular inductor model shown in Fig. 16(a) is a CM inductor with the winding structure (e) in Fig. 11. The baseline inductor model shown in Fig. 16(b) includes two paralleled concentric cores. Regular windings are wound on the two parallel cores in comparison with the proposed structure. The proposed CM inductor model in Fig. 16(c) has two cores with the proposed winding structure as shown in Fig. 14 and meets condition (9). The wire size used in the simulation is AWG# 22 (0.645 mm diameter), the same

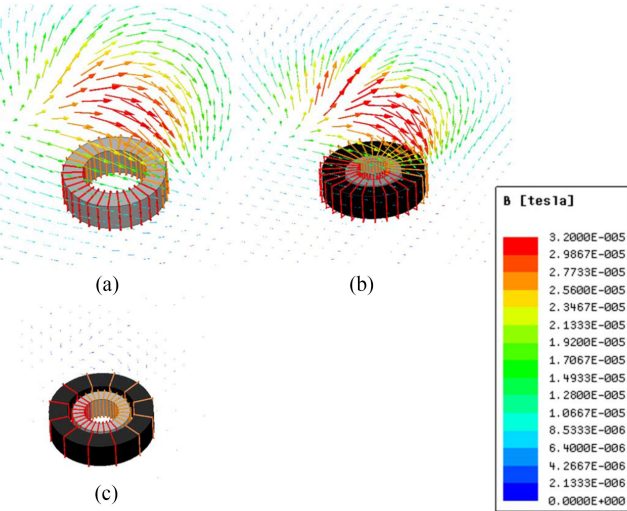


Fig. 16. Simulated near magnetic field emission on a horizontal plane 20 mm above the inductors. (a) Regular CM inductor. (b) Baseline inductor. (c) Proposed CM inductor.

as used in the experiments. DM dc current of 5 A was added as excitation.

As discussed in Section II, the main source of near magnetic field emission of a CM inductor is the leakage flux due to DM excitation. Because of this, the near magnetic field emission generated by the equivalent winding loop around the core can be ignored. It is shown in Fig. 16 that the proposed CM inductors have much smaller near magnetic field emission than the regular and baseline CM inductors.

B. Increased DM Inductance

In Fig. 15, the DM magnetic flux that is generated by DM current I_{DM} approximately meets the following condition:

$$2\Phi_A \approx 2\Phi_B \approx \Phi_{\text{gap}} \approx \frac{F_A + F_B}{\frac{R_{\text{core}A}}{4} + R_{\text{gap}} + \frac{R_{\text{core}B}}{4}}. \quad (15)$$

The DM inductance is therefore given as follows:

$$L_{\text{DM}} = \frac{2(N_A + N_B)\Phi_A}{I_{\text{DM}}} = \frac{(N_A + N_B)^2}{\frac{R_{\text{core}A}}{4} + R_{\text{gap}} + \frac{R_{\text{core}B}}{4}}. \quad (16)$$

It is much larger than that in (5) of a conventional CM inductor because magnetic flux $2\Phi_A$ is much bigger than $2(\Phi_1 + \Phi_{\text{air}C})$ in (4). The conventional CM inductor in Fig. 6 has a high reluctance $R_{\text{air}}//R_{\text{air}C}$ for DM magnetic flux, so DM inductance is small. The proposed CM inductor in Fig. 15 has a much smaller reluctance $R_{\text{gap}} + (R_{\text{core}A} + R_{\text{core}B})/4$ than $R_{\text{air}}//R_{\text{air}C}$, so its DM inductance is greatly increased. The reason is that the two cores and the small air gaps between them provide small reluctance paths for DM magnetic flux. The DM inductances on two cores are closely and directly coupled.

Simulation were conducted for the three CM inductors in Table II. The simulated DM inductance is 3.6 μH for the regular CM inductor, 2.4 μH for the baseline CM inductor, and 12.8 μH for the proposed CM inductor. This validates that the proposed inductor structure has much higher DM inductance than conventional CM inductor structures.

In Table II, the saturation of the cores depends on the total flux from the DM and CM currents. The design procedure presented

in Section IV-C will guarantee the cores of the proposed inductor will not be saturated under rated operating conditions. The temperature measurement in Section V will show that compared with the regular CM inductor, the proposed CM inductor has only a small temperature rising at rated working condition. Therefore, the thermal is not an issue.

C. Inductor Design to Achieve Desired Inductance, Near Magnetic Field Cancellation, and Unsaturated Core

The proposed CM inductor should not only meet CM inductance, increased DM inductance, and reduced near magnetic field requirements but also optimal magnetic flux density requirement.

There are three most important constraints when designing the proposed CM inductor.

- 1) Required CM inductance: The CM inductance should meet (17); because most of the CM magnetic flux is inside the cores, and the mutual inductance between the windings on cores A and B is ignored in (17).
- 2) Total near magnetic flux cancellation: It means condition (9) must be satisfied.
- 3) The magnetic flux density in cores A and B cannot be too high or too low: Under the worst scenario when the CM and DM fluxes are added together, the magnetic flux density of two cores should be smaller than 0.9 times of the saturation flux density but larger than half of saturation flux density at the highest operating temperature, as shown in (18) and (19)

$$L_{\text{CM}} = \frac{N_A^2}{R_{\text{core}A}} + \frac{N_B^2}{R_{\text{core}B}} \quad (17)$$

$$0.5 B_{\text{sat}A} \leq \frac{\Phi_{\text{CMA}}}{A_A} + \frac{\Phi_A}{A_A} \leq 0.9 B_{\text{sat}A} \quad (18)$$

$$0.5 B_{\text{sat}B} \leq \frac{\Phi_{\text{CMB}}}{A_B} + \frac{\Phi_B}{A_B} \leq 0.9 B_{\text{sat}B} \quad (19)$$

where $B_{\text{sat}A}$ and $B_{\text{sat}B}$ are saturation flux density of the core A and core B, respectively. Φ_A and Φ_B are given as (15), representing the magnetic flux inside the cores A and B due to DM current excitation. Φ_{CMA} and Φ_{CMB} are CM flux inside core A and core B due to CM current I_{CM} excitation, respectively, and are given as follows;

$$\Phi_{\text{CMA}} = \frac{2N_A I_{\text{CM}}}{R_{\text{core}A}} \quad (20)$$

$$\Phi_{\text{CMB}} = \frac{2N_B I_{\text{CM}}}{R_{\text{core}B}}. \quad (21)$$

Based on (9) and (17)–(21), N_A and N_B can be eliminated as shown in (22) and (23), which leaves only core dimensions and design specifications

$$\begin{aligned} \frac{B_{\text{sat}A}^2}{16L_{\text{CM}}} &\leq \frac{R_{\text{core}B} \cdot (I_{\text{CM}} + I_{\text{DM}})^2}{A_A^2 \left[R_{\text{core}A} R_{\text{core}B} + (R_{\text{core}B} + 4R_{\text{gap}})^2 \right]} \\ &\leq \frac{B_{\text{sat}A}^2}{4.94L_{\text{CM}}} \end{aligned} \quad (22)$$

Once the cores are selected, (22) and (23) as shown at the bottom of this page, can be used to determine whether the magnetic flux density is optimal in core A and core B based

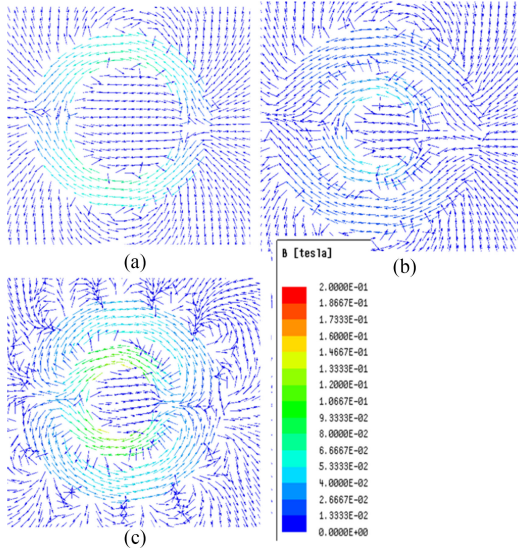


Fig. 17. Simulated near magnetic field emission on a plane across the inductors. (a) Regular CM inductor. (b) Baseline inductor. (c) Proposed CM inductor.

on their dimensions and design specifications, respectively. If the conditions (22) and (23) are satisfied, then the core's magnetic flux density is optimal, otherwise the cores' magnetic flux density is either too high or too low. The number of winding turns on core A and core B can be solved from (9) and (17). In (22) and (23), if the calculated value is smaller than the lower limit, the core will saturate under the rated currents. A core with larger cross-sectional area should be used. If the calculated value is bigger than the upper limit, the inductor is over designed. A core with smaller cross-sectional area should be selected.

In this article, $I_{DM} = 5$ A, $I_{CM} = 50$ mA, and the saturation flux density was 0.2 T at 100 °C. The core dimensions and number of winding turns are shown in Table II. Three inductors in Table II were designed. All these inductors have a CM inductance of 530 μH. The regular CM inductor is a conventional inductor with winding structure (e). The proposed CM inductor is an inductor with the proposed winding structure and meets the conditions (9), (17)–(23). The baseline CM inductor is an inductor with conventional winding structure (e) but with two parallel concentric cores, as shown in Fig. 16(b). The two cores are the same as those used in the proposed inductor for a fair comparison.

Simulations were conducted under the worst condition where the maximum rated currents were added to the windings. The flux density inside the cores is shown in Fig. 17. It is shown that the flux density inside all the cores falls into the desired 0.5 B_{sat} to 0.9 B_{sat} range.

To verify the core in the proposed CM inductor is not saturated under rated DM current so the CM inductance of the proposed CM inductor is not reduced, the CM impedance of the proposed CM inductor with the dimensions presented in Table II is measured under 0 A and rated 5 A DM current bias in Fig. 18(a) for a developed prototype. In Fig. 18(a), the two-port S-parameters were first measured using a copper mountain PLANAR 808/1 network analyzer, and the CM impedance were derived from

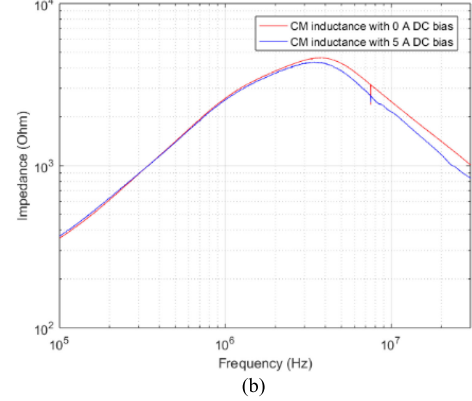
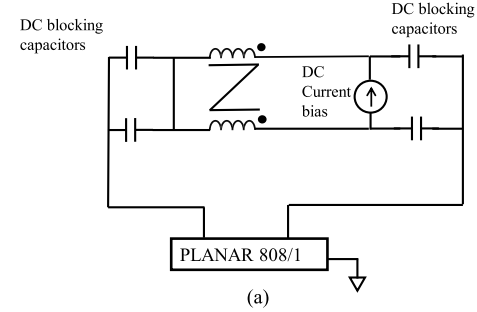


Fig. 18. CM impedance of the proposed CM inductor under 0 A and 5 A dc current bias. (a) S-parameter measurement setup (b) Derived CM impedance curves.

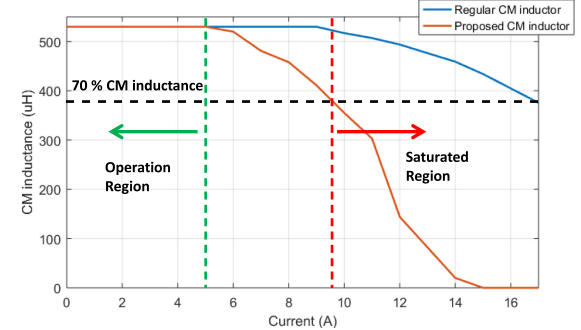


Fig. 19. CM inductance comparison between the regular and proposed CM inductors at different DM currents.

the measured S-parameters [23]. The CM impedance curves are shown in Fig. 18(b). As expected, the CM impedance of the proposed CM inductor does not change much after the change of DM current bias from 0 A to the rated 5 A dc current bias.

It should be pointed out that because the reluctance of the proposed CM inductor to DM flux is smaller than that of the regular CM inductor, the DM saturation current of the proposed CM inductor is lower than that of the regular CM inductor. The CM inductance can be reduced when the core is saturated by the DM current. The measured CM inductances of regular and proposed CM inductor under different DM currents are compared in Fig. 19. As shown in Fig. 19, both CM inductors are not saturated under rated 5 A DM current, which is the designed maximum DM current for the proposed CM inductor. After DM

$$\frac{B_{satB}^2}{16L_{CM}} \leq \frac{I_{CM}^2 \cdot (R_{coreB} + 4R_{gap})^2 + I_{DM}^2 \cdot R_{coreB}^2 + 2I_{CM} \cdot I_{DM} \cdot R_{coreB} \cdot (R_{coreB} + 4R_{gap})}{A_B^2 \cdot R_{coreB}} \leq \frac{B_{satB}^2}{4.94L_{CM}} \quad (23)$$

current is higher than 5 A, the proposed CM inductor begins to saturate. On the other hand, the regular CM inductor does not saturate until 9 A. When the CM inductance is reduced to 70% of the unsaturated value, the DM current in the proposed CM inductor is 9.6 A, and the DM current in the regular CM inductor is 17 A. In the proposed CM inductor, when the DM current is higher than the rated value, core A will saturate first due to its smaller cross-sectional area. Because core B has a cross-sectional area 2.2 times of core A, it will not saturate until 11 A. After that, both cores are saturated, and the CM inductance will quickly fall to zero. For the regular CM inductor, because most of the DM magnetic flux flows through air, it has higher DM saturation current, which is good, but also higher near magnetic field emission, which is bad, than the proposed one.

Because of the reasons discussed in the previous paragraph, it is very important to follow the design procedure proposed in this section to prevent core saturation when employing the proposed CM inductor.

V. EXPERIMENTAL VERIFICATIONS

In this section, the analysis of near magnetic field emissions from inductors (a)–(g) in Figs. 8 and 11 is first validated with experiments. Second, the analysis of the near magnetic field emissions from regular conventional CM inductors and the proposed CM inductor in Section IV is validated via measurements. Conducted EMI is measured for a boost converter with the regular and proposed CM inductors as EMI filter component is compared.

DM inductors (a)–(d) use powder cores with relative permeability of 60. Inner diameter is 13.7 mm, and outer diameter is 24.4 mm. Core height is 9.66 mm. The total number of winding turns is 20. All the measured DM inductances are close to 20 μH . CM inductors (e)–(g) use ferrite cores with relative permeability of 5000. Inner diameter is 13.7 mm, and outer diameter is 22.1 mm. Core height is 6.35 mm. The total number of turns of each winding is 10. All the measured CM inductances are close to 200 μH . AWG# 24 (wire diameter 0.51 mm) is used for the winding wires of all the inductors.

A signal generator RIGOL DS 1052E, a Beehive Electronics 100-C EMC probe, a 25-W RF amplifier (model 25A250A), and a Rohde & Schwarz FSH4 spectrum analyzer were used in near magnetic field measurements. The experiment setup is shown in Fig. 20. The inductors were placed under the center of a coordinated board. The distance between the coordinated board and the inductors was 20 mm and can be adjusted to compensate the radius of the EMC probe. A 150-kHz sinusoidal voltage signal was generated by the signal generator and amplified by the RF amplifier. The amplified signal was fed to the inductor.

A current probe was used to monitor the input DM current to make sure it is 2 A. The coordinated board has $14 \times 14 = 196$ points on a 7.5-mm spaced grid. The EMC probe was connected to the spectrum analyzer to measure the magnetic flux density B_x , B_y , and B_z in x -, y -, and z -direction at each point. The measured data were converted to magnetic flux density B in Tesla based on EMC probe's data sheet, and the total magnetic flux density was calculated based on the following equation:

$$B = \sqrt{B_x^2 + B_y^2 + B_z^2}. \quad (24)$$

The measured near magnetic field distributions for inductors (a)–(d) are shown in Fig. 21. As shown in Fig. 21,

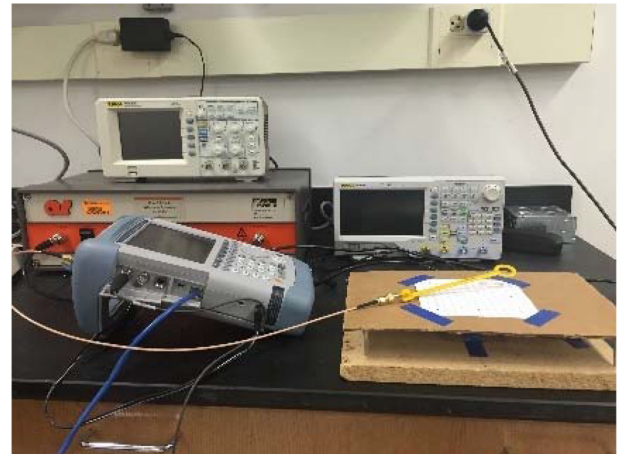


Fig. 20. Experiment setup for near magnetic field measurement.

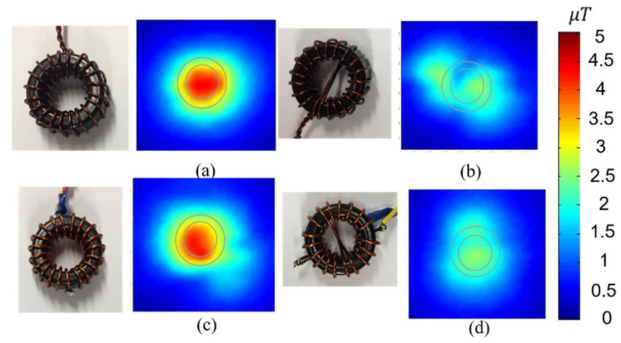


Fig. 21. Measured near magnetic field for the DM inductors (a), (b), (c), and (d) in Fig. 8 on a plane 20 mm above the inductors with 1.5 A DM current excitation.

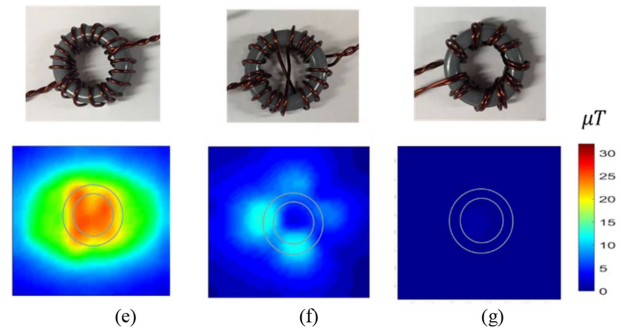


Fig. 22. Measured near magnetic field for the CM inductors (e), (f), and (g) in Fig. 11 on a plane 20 mm above the inductors with 1.5 A DM current excitation.

inductor (a) has a similar near magnetic field emission to inductor (c). At the same time, inductor (b) has a similar near magnetic field emission to inductor (d). The near magnetic field emission of inductors (b) and (d) is lower than that of inductors (a) and (c). This validated the analysis presented in Section III-A.

The measured near magnetic field distributions for inductors (e)–(g) are shown in Fig. 22. As shown in Fig. 22, inductor (e) has the highest near magnetic field emission. The near magnetic field of inductor (f) is much smaller than that of inductor (e). Inductor (g) has the smallest near magnetic field emission. The measured DM inductance for inductors (e)–(g) is 1.46, 0.64,

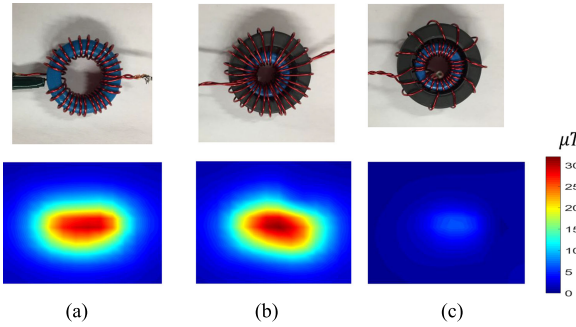


Fig. 23. Inductor prototypes and measured near magnetic field distributions on a plane 20 mm above the inductors. (a) Regular. (b) Baseline. (c) Proposed.

and 0.18, μH respectively. All of these validated the analysis presented in Section III-B.

To validate the analysis of the near magnetic field emissions from a regular CM inductor and the proposed CM inductor in Section IV, three CM inductor prototypes were developed and are shown in Fig. 23. The inductors have the same parameter as presented in Table II. The wire used for windings is AWG# 22 (wire diameter 0.645 mm), which is chosen according to the current rating. Core A uses EPCOS B64290L45X830, and regular inductor core uses EPCOS B64290L0638X830. Core B uses Fair-rite 5967001001.

The measured near magnetic field distributions are also shown in Fig. 23. Compared with the regular and baseline CM inductors, the proposed CM inductor reduced the near magnetic field emission by more than 80%. This verified the analysis presented in Section IV.

The measured CM impedances and DM impedances are compared in Fig. 24. At low frequencies, all inductors have a CM inductance close to 530 μH . The proposed CM inductors have bigger CM impedance than the regular CM inductor at high frequencies above 2 MHz because the inner and outer inductors' high-frequency resonant frequencies, which is caused by the inductance and winding capacitance, are separated, which results in a wider bandwidth than conventional CM inductor structures. It therefore has a better performance than the conventional inductors for high-frequency CM noise reduction. The measured DM inductance is 5.2 μH for regular one, 4.7 μH for baseline one, and 10.1 μH for the proposed one. All of this validated the analysis presented in Section IV.

The regular and the proposed inductors were used as a filter inductor of a boost converter, and the conducted EMI is measured. Fig. 25 shows the measurement setup. Two L-type EMI filters were developed for these two inductors, and both of them have two 1 nF CM capacitors and one 0.1 μF DM capacitor, as shown in Fig. 25. To evaluate the inductor's performance, the filter component layout is the same as that popularly used in commercial products in Fig. 26. The regular CM inductor shown in Fig. 23 is used in filter 1, and the proposed CM inductor shown in Fig. 23 is used in filter 2.

Because this article focuses on inductor design and its near-field emission, measurements were only conducted to compare the performance of the filters with different inductors and to verify the analysis in this article. For a specific application, EMI filters must be carefully designed. A lot of research has been done for EMI filter design so this article will not repeat it. The proposed CM inductor structure can be applied to any EMI filters.

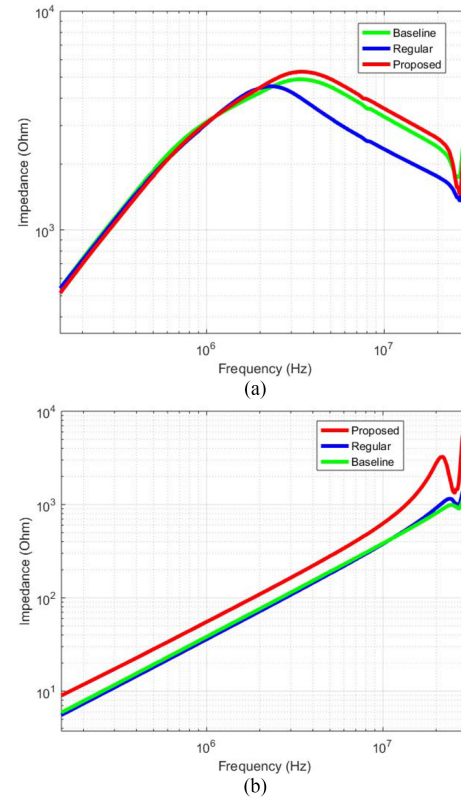


Fig. 24. Measured impedances for CM inductors. (a) CM impedance. (b) DM impedance.

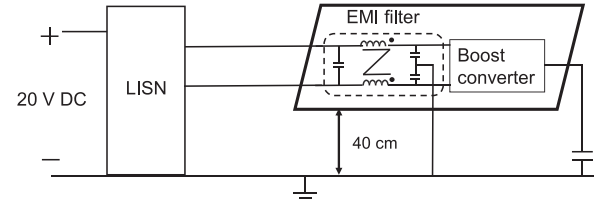


Fig. 25. EMI measurement setup with inductors used as filter inductors in a boost converter.

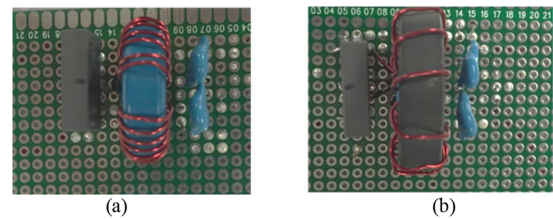


Fig. 26. EMI filters with regular and the proposed CM inductor. (a) With a regular CM inductor. (b) With a proposed CM inductor.

The CM and DM insertion gain S21 of the two EMI filters are first measured with copper mountain PLANAR 808/1 network analyzer under the rated 5 A dc current bias. The setups for CM and DM insertion gain measurement are shown in Fig. 27(a) and (b). The rated 5 A current bias is added to the windings via a current source. In the CM insertion gain measurement setup, four 1 μF ceramic dc blocking capacitors are used to isolate the network analyzer from the current source.

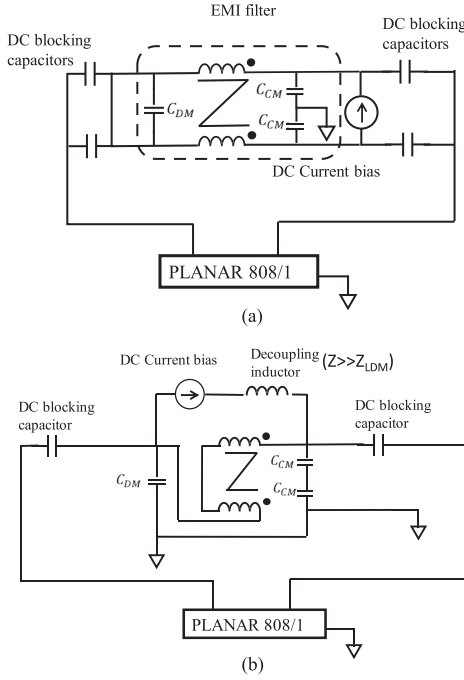


Fig. 27. S-parameter measurement setup under 0 and 5 A dc current bias for (a) CM filter insertion gain measurement and (b) DM filter insertion gain measurement.

The self-resonant frequency of the four capacitors is above 30 MHz so the capacitor's parasitic inductance does not influence the measurement results. The series resonant frequency between the dc blocking capacitors and CM inductance is 7 kHz, which is far below 150 kHz, so the impedance of the dc blocking capacitors does not influence the measured CM impedance above 150 kHz. Similarly, in the DM insertion gain measurement setup, two 1 μ F ceramic dc blocking capacitors are used to isolate the network analyzer from the current source. The impedance of the decoupling inductor is much higher than that of the DM inductor, which is the leakage inductance of the CM inductor, from 150 kHz to 30 MHz. The two windings are reversely in series so only the DM impedance of leakage inductance is measured. It should be noted that the measured CM and DM insertion gains of EMI filters are based on 50 Ω source and load impedance. In real converter circuits, the source and load impedance of the filters are not 50 Ω [23]. In addition, the S-parameter measurement does not reflect the possible near-field coupling between the filters components and power delivery paths connected to the filters. Because of this, the measured insertion gains are not supposed to be identical to the in-circuit EMI measurement results.

The insertion gains were measured under 5 A dc bias using a copper mountain PLANAR 808/1 network analyzer shown in Fig. 28. In Fig. 28(a), the CM insertion gains of the two filters are very similar at low frequencies. At high frequencies above 2 MHz, because the proposed CM inductor has bigger CM impedance, as shown in Fig. 24, the insertion gain of the filter with the proposed CM inductor is better (lower). For DM insertion gains, the proposed inductor has higher DM inductance, so the first corner frequency is lower and low-frequency insertion gain is better. At high frequencies, the filter with the proposed CM inductor has much lower near magnetic field emission than the conventional CM inductor, so the inductive

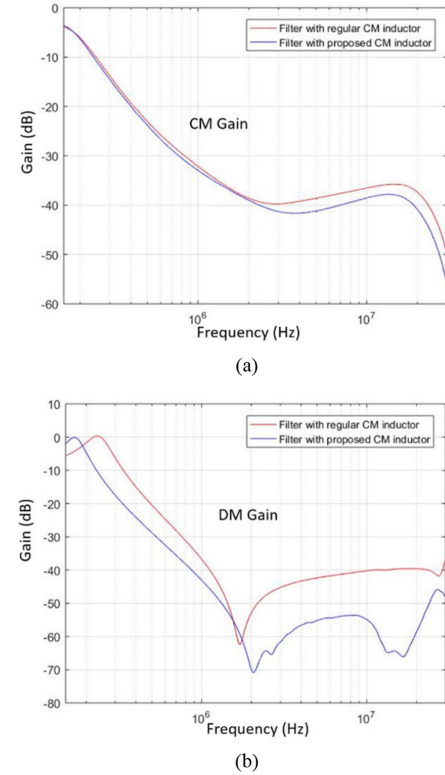


Fig. 28. Comparison of the measured insertion gain of EMI filters. (a) CM gain. (b) DM gain.

coupling between the inductor and capacitors is much smaller than the conventional inductor [1], [3]. As a result, the filter with the proposed CM inductor has much better high-frequency performance than the filter with the conventional CM inductor. Once again, it should be pointed out that, in actual applications, the source and load impedance of the EMI filter in the converter is not 50 Ω , so the actual performance improvement and corner frequencies will be different from those presented in Fig. 28(a) and (b) [23], [24], but the measurement in Fig. 28 can still prove the performance improvement with the proposed inductor.

The in-circuit performance of the two EMI filters in Fig. 26 is tested in Fig. 25 in a boost PFC converter, and the measured CM and DM noise spectra are compared in Fig. 29.

As shown in Fig. 29(a), with the proposed CM inductor, CM noise can be reduced by around 10 dB than that using the regular CM inductor above 2 MHz due to the increased high-frequency impedance. Other than the parasitic couplings between two filter components elaborated in [15] and [16], the emitted near magnetic field due to the DM current in a regular CM inductor could also induce noise voltage in the input power delivery path, as described in [5]. For the proposed CM inductor, due to the minimized near magnetic field, there is very small induced noise voltages in the input power delivery path. In Fig. 29(b), the DM noise can be reduced by up to 22 dB with the proposed CM inductor than that using the regular CM inductor due to the increased DM inductance and the minimized near magnetic field couplings between the inductor and other components.

There is a small sacrifice for the proposed CM inductor to achieve the desired high performance. First, longer winding wires are needed, which could increase conduction power loss.

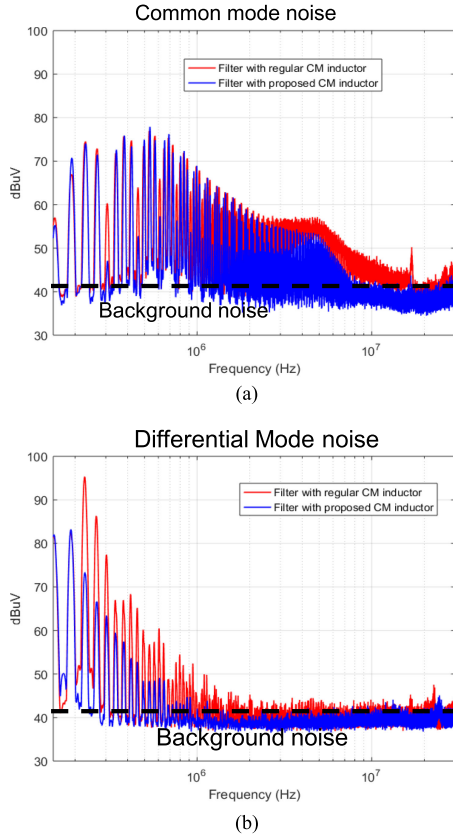


Fig. 29. Comparison of the measured EMI noise. (a) CM. (b) DM.

Also, the proposed CM inductor structure increases the footprint of the EMI filter by 8% in the experiments. However, since the regular CM inductor achieves smaller EMI attenuation than the proposed one, the EMI filter with the regular CM inductor may need additional filter components, such as inductors or capacitors to achieve the same performance as the filter with the proposed inductor. As a result, the footprint, power loss, and

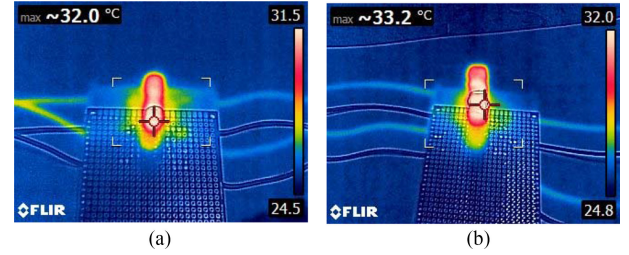


Fig. 30. Comparison of the steady-state temperatures. (a) Regular CM inductor. (b) Proposed CM inductor.

the cost of the filter with the regular inductor may still be higher than that with the proposed inductor.

Because longer winding wires are used for the proposed inductor than the regular one, more conduction power loss is generated. It is therefore necessary to guarantee the proposed CM inductor does not have thermal issues. In Fig. 29, the steady-state temperatures of both CM inductors were measured with an FLIR thermal camera.

In Fig. 30, the measured maximum temperature of the regular CM inductor is 32.0 °C, and the maximum temperature of the proposed CM inductor is 33.2 °C. Therefore, the thermal is not an issue in this case.

It should be pointed out that proposed inductor structure can be easily implemented using two individual concentric inductors with their winding terminals soldered to printed circuit board (PCB). The two inductors do not need to be directly connected using winding wires. They can be connected using PCB traces. Because of this, there is no massive production issue.

VI. CONCLUSION

In this article, the mechanism of near magnetic field emission and near magnetic field distribution is analyzed for different inductor winding structures. The research was conducted for both DM and CM inductors with CM or DM current excitation. The winding structures with small near magnetic field emission are identified. The advantages and disadvantages of

$$B_{x_{i1}} = \frac{\mu_0 I}{4\pi} \cdot \frac{-(z + \frac{H}{2}) \cos \theta_i}{\sqrt{(x \cos \theta_i - y \sin \theta_i)^2 + (z + \frac{H}{2})^2} \sqrt{x^2 + y^2 - (x \sin \theta_i + y \cos \theta_i)^2}} \\ \cdot \left(\frac{\sqrt{x \sin \theta_i + y \cos \theta_i} + r}{r_2} - \frac{\sqrt{x \sin \theta_i + y \cos \theta_i} + R}{r_3} \right) \quad (A1)$$

$$B_{y_{i1}} = \frac{\mu_0 I}{4\pi} \cdot \frac{-(z + \frac{H}{2}) \sin \theta_i}{\sqrt{(x \cos \theta_i - y \sin \theta_i)^2 + (z + \frac{H}{2})^2} \sqrt{x^2 + y^2 - (x \sin \theta_i + y \cos \theta_i)^2}} \\ \cdot \left(\frac{\sqrt{x \sin \theta_i + y \cos \theta_i} + r}{r_2} - \frac{\sqrt{x \sin \theta_i + y \cos \theta_i} + R}{r_3} \right) \quad (A2)$$

$$B_{z_{i1}} = \frac{\mu_0 I}{4\pi} \cdot \frac{-y \sin \theta_i + x \cos \theta_i}{\sqrt{(x \cos \theta_i - y \sin \theta_i)^2 + (z + \frac{H}{2})^2} \sqrt{x^2 + y^2 - (x \sin \theta_i + y \cos \theta_i)^2}} \\ \cdot \left(\frac{\sqrt{x \sin \theta_i + y \cos \theta_i} + r}{r_2} - \frac{\sqrt{x \sin \theta_i + y \cos \theta_i} + R}{r_3} \right) \quad (A3)$$

these winding structures are discussed. A new CM inductor structure is proposed to reduce near magnetic field emission and increase DM inductance at the expense of reduced DM saturation current. Its working principle is analyzed in detail. A design procedure is developed for the proposed inductor structure to achieve minimized near magnetic field emission, increased DM inductance, desired CM inductance, and optimal magnetic flux density inside the cores. Both simulations and experiments were conducted to validate the analysis and theory developed in this article. EMI measurements were conducted to validate that the proposed inductor can improve EMI filter performance and reduce both DM and CM EMI noise. Although this article focuses on toroidal inductors, the proposed flux cancellation technique can also be applied to inductors or transformers with different core shapes.

APPENDIX

To calculate the magnetic field outside a rectangular current loop, the PEEC method is used [20]. According to the superposition principle, the total magnetic flux density at point P is the sum of magnetic flux density generated by each current segment. A single winding turn can be represented by a rectangular current loop, as shown in Fig. 31. The rectangular current loop is divided into four segments, 1–4.

As shown in Fig. 31, θ_i represents the position angle of the i th current loop. With N -turn current loops evenly distributed on the core, $\theta_i = i \cdot \frac{360^\circ}{N}$. The magnetic flux density of current loop i can be calculated by adding magnetic flux density generated by current segment 1 to 4.

The inner radius of the core is represented by r , whereas the outer radius is R . The windings are assumed evenly distributed on the core and positioned closely. The height of the core is H , which is not noted in Fig. 31, and the diameter of winding wire is ignored.

The magnetic field flux density at point P generated by current segment 1 can be calculated with Biot–Savart's law in xyz dimensions (A1)–(A3) shown at the bottom of previous page.

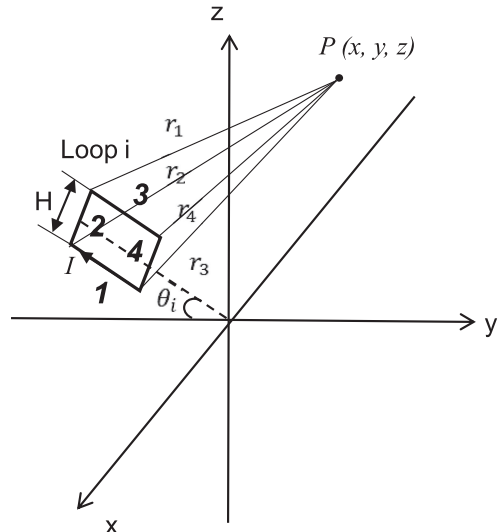


Fig. 31. Magnetic field flux density outside of a rectangular current loop.

In a similar way, the flux density generated by the other three current segments can also be calculated in xyz dimensions

$$B_{x_{i2}} = \frac{\mu_0 I}{4\pi} \cdot \frac{-y - R \cos \theta_i}{(x + R \sin \theta_i)^2 + (y + R \cos \theta_i)^2} \cdot \left(\frac{z - \frac{H}{2}}{r_1} - \frac{z + \frac{H}{2}}{r_2} \right) \quad (\text{A4})$$

$$B_{y_{i2}} = \frac{\mu_0 I}{4\pi} \cdot \frac{-x - R \sin \theta_i}{(x + R \sin \theta_i)^2 + (y + R \cos \theta_i)^2} \cdot \left(\frac{z - \frac{H}{2}}{r_1} - \frac{z + \frac{H}{2}}{r_2} \right) \quad (\text{A5})$$

$$B_{z_{i2}} = 0 \quad (\text{A6})$$

$$B_{x_{i3}} = \frac{\mu_0 I}{4\pi} \cdot \frac{-(z - \frac{H}{2}) \cos \theta_i}{\sqrt{(x \cos \theta_i - y \sin \theta_i)^2 + (z - \frac{H}{2})^2} \sqrt{x^2 + y^2 - (x \sin \theta_i + y \cos \theta_i)^2}} \cdot \left(\frac{\sqrt{x \sin \theta_i + y \cos \theta_i} + r}{r_4} - \frac{\sqrt{x \sin \theta_i + y \cos \theta_i} + R}{r_1} \right) \quad (\text{A7})$$

$$B_{y_{i3}} = \frac{\mu_0 I}{4\pi} \cdot \frac{-(z - \frac{H}{2}) \sin \theta_i}{\sqrt{(x \cos \theta_i - y \sin \theta_i)^2 + (z - \frac{H}{2})^2} \sqrt{x^2 + y^2 - (x \sin \theta_i + y \cos \theta_i)^2}} \cdot \left(\frac{\sqrt{x \sin \theta_i + y \cos \theta_i} + r}{r_4} - \frac{\sqrt{x \sin \theta_i + y \cos \theta_i} + R}{r_1} \right) \quad (\text{A8})$$

$$B_{z_{i3}} = \frac{\mu_0 I}{4\pi} \cdot \frac{-y \sin \theta_i + x \cos \theta_i}{\sqrt{(x \cos \theta_i - y \sin \theta_i)^2 + (z - \frac{H}{2})^2} \sqrt{x^2 + y^2 - (x \sin \theta_i + y \cos \theta_i)^2}} \cdot \left(\frac{\sqrt{x \sin \theta_i + y \cos \theta_i} + r}{r_4} - \frac{\sqrt{x \sin \theta_i + y \cos \theta_i} + R}{r_1} \right) \quad (\text{A9})$$

Equations (A7)–(A9) shown at the bottom of previous page.

$$B_{x_{i4}} = \frac{\mu_0 I}{4\pi} \cdot \frac{-y - r \cos \theta_i}{(x + r \sin \theta_i)^2 + (y + r \cos \theta_i)^2} \cdot \left(\frac{z + \frac{H}{2}}{r_3} - \frac{z - \frac{H}{2}}{r_4} \right) \quad (\text{A10})$$

$$B_{y_{i4}} = \frac{\mu_0 I}{4\pi} \cdot \frac{-x - r \sin \theta_i}{(x + r \sin \theta_i)^2 + (y + r \cos \theta_i)^2} \cdot \left(\frac{z + \frac{H}{2}}{r_3} - \frac{z - \frac{H}{2}}{r_4} \right) \quad (\text{A11})$$

$$B_{z_{i4}} = 0 \quad (\text{A12})$$

where

$$r_1 = \sqrt{(x + R \sin \theta_i)^2 + (y + R \cos \theta_i)^2 + \left(z - \frac{H}{2}\right)^2} \quad (\text{A13})$$

$$r_2 = \sqrt{(x + R \sin \theta_i)^2 + (y + R \cos \theta_i)^2 + \left(z + \frac{H}{2}\right)^2} \quad (\text{A14})$$

$$r_3 = \sqrt{(x + r \sin \theta_i)^2 + (y + r \cos \theta_i)^2 + \left(z + \frac{H}{2}\right)^2} \quad (\text{A15})$$

$$r_4 = \sqrt{(x + r \sin \theta_i)^2 + (y + r \cos \theta_i)^2 + \left(z - \frac{H}{2}\right)^2}. \quad (\text{A16})$$

The total magnetic flux density of an inductor consist of N winding turns can be calculated by applying the superposition principle, as shown in Fig. 32.

The flux density at point P due to each current segment of all the current loops can be calculated from the following equations (A17)–(A19) shown at the bottom of this page:

$$B_{x_{2\text{total}}} = \frac{\mu_0 I}{4\pi} \cdot \sum_{i=1}^N \frac{-y - R \cos \theta_i}{(x + R \sin \theta_i)^2 + (y + R \cos \theta_i)^2} \cdot \left(\frac{z - \frac{H}{2}}{r_{1i}} - \frac{z + \frac{H}{2}}{r_{2i}} \right) \quad (\text{A20})$$

$$B_{y_{2\text{total}}} = \frac{\mu_0 I}{4\pi} \cdot \sum_{i=1}^N \frac{-x - R \sin \theta_i}{(x + R \sin \theta_i)^2 + (y + R \cos \theta_i)^2} \cdot \left(\frac{z - \frac{H}{2}}{r_{1i}} - \frac{z + \frac{H}{2}}{r_{2i}} \right) \quad (\text{A21})$$

$$B_{z_{2\text{total}}} = 0 \quad (\text{A22})$$

Equations (A23)–(A25) shown at the bottom of this page.

$$B_{x_{4\text{total}}} = \frac{\mu_0 I}{4\pi} \cdot \sum_{i=1}^N \frac{-y - r \cos \theta_i}{(x + r \sin \theta_i)^2 + (y + r \cos \theta_i)^2} \cdot \left(\frac{z + \frac{H}{2}}{r_{3i}} - \frac{z - \frac{H}{2}}{r_{4i}} \right) \quad (\text{A26})$$

$$B_{x_{1\text{total}}} = \frac{\mu_0 I}{4\pi} \cdot \sum_{i=1}^N \frac{-(z + \frac{H}{2}) \cdot \cos \theta_i \cdot \left(\frac{\sqrt{x \sin \theta_i + y \cos \theta_i} + r}{r_{2i}} - \frac{\sqrt{x \sin \theta_i + y \cos \theta_i} + R}{r_{3i}} \right)}{\sqrt{(x \cos \theta_i - y \sin \theta_i)^2 + (z + \frac{H}{2})^2} \left(x^2 + y^2 - (x \sin \theta_i + y \cos \theta_i)^2 \right)} \quad (\text{A17})$$

$$B_{y_{1\text{total}}} = \frac{\mu_0 I}{4\pi} \cdot \sum_{i=1}^N \frac{-(z + \frac{H}{2}) \cdot \sin \theta_i \cdot \left(\frac{\sqrt{x \sin \theta_i + y \cos \theta_i} + r}{r_{2i}} - \frac{\sqrt{x \sin \theta_i + y \cos \theta_i} + R}{r_{3i}} \right)}{\sqrt{(x \cos \theta_i - y \sin \theta_i)^2 + (z + \frac{H}{2})^2} \left(x^2 + y^2 - (x \sin \theta_i + y \cos \theta_i)^2 \right)} \quad (\text{A18})$$

$$B_{z_{1\text{total}}} = \frac{\mu_0 I}{4\pi} \cdot \sum_{i=1}^N \frac{(-y \sin \theta_i + x \cos \theta_i) \cdot \left(\frac{\sqrt{x \sin \theta_i + y \cos \theta_i} + r}{r_{2i}} - \frac{\sqrt{x \sin \theta_i + y \cos \theta_i} + R}{r_{3i}} \right)}{\sqrt{(x \cos \theta_i - y \sin \theta_i)^2 + (z + \frac{H}{2})^2} \left(x^2 + y^2 - (x \sin \theta_i + y \cos \theta_i)^2 \right)} \quad (\text{A19})$$

$$B_{x_{3\text{total}}} = \frac{\mu_0 I}{4\pi} \cdot \sum_{i=1}^N \frac{-(z - \frac{H}{2}) \cos \theta_i \cdot \left(\frac{\sqrt{x \sin \theta_i + y \cos \theta_i} + r}{r_{4i}} - \frac{\sqrt{x \sin \theta_i + y \cos \theta_i} + R}{r_{1i}} \right)}{\sqrt{(x \cos \theta_i - y \sin \theta_i)^2 + (z - \frac{H}{2})^2} \left(x^2 + y^2 - (x \sin \theta_i + y \cos \theta_i)^2 \right)} \quad (\text{A23})$$

$$B_{y_{3\text{total}}} = \frac{\mu_0 I}{4\pi} \cdot \sum_{i=1}^N \frac{-(z - \frac{H}{2}) \sin \theta_i \cdot \left(\frac{\sqrt{x \sin \theta_i + y \cos \theta_i} + r}{r_{4i}} - \frac{\sqrt{x \sin \theta_i + y \cos \theta_i} + R}{r_{1i}} \right)}{\sqrt{(x \cos \theta_i - y \sin \theta_i)^2 + (z - \frac{H}{2})^2} \left(x^2 + y^2 - (x \sin \theta_i + y \cos \theta_i)^2 \right)} \quad (\text{A24})$$

$$B_{z_{3\text{total}}} = \frac{\mu_0 I}{4\pi} \cdot \sum_{i=1}^N \frac{(-y \sin \theta_i + x \cos \theta_i) \cdot \left(\frac{\sqrt{x \sin \theta_i + y \cos \theta_i} + r}{r_{4i}} - \frac{\sqrt{x \sin \theta_i + y \cos \theta_i} + R}{r_{1i}} \right)}{\sqrt{(x \cos \theta_i - y \sin \theta_i)^2 + (z - \frac{H}{2})^2} \left(x^2 + y^2 - (x \sin \theta_i + y \cos \theta_i)^2 \right)} \quad (\text{A25})$$

$$B_{x_{1\text{total}_k}} = \frac{\mu_0 I}{4\pi} \cdot \frac{-(z + \frac{H}{2}) \cdot \cos \theta_k \cdot \left(\frac{\sqrt{x \sin \theta_k + y \cos \theta_k} + r}{r_{2k}} - \frac{\sqrt{x \sin \theta_k + y \cos \theta_k} + R}{r_{3k}} \right)}{\sqrt{\left((x \cos \theta_k - y \sin \theta_k)^2 + (z + \frac{H}{2})^2 \right) \left(x^2 + y^2 - (x \sin \theta_k + y \cos \theta_k)^2 \right)}} \quad (\text{A38})$$

$$B_{x_{1\text{total}_{k\&j}}} = \frac{\mu_0 I}{4\pi} \cdot \frac{-(z + \frac{H}{2}) \cdot \cos \theta_k \cdot \left(\begin{array}{l} \left(\frac{\sqrt{x \sin \theta_k + y \cos \theta_k} + r}{r_{2k}} - \frac{\sqrt{x \sin \theta_k + y \cos \theta_k} + R}{r_{2j}} \right) \\ - \left(\frac{\sqrt{x \sin \theta_k + y \cos \theta_k} + R}{r_{3k}} - \frac{\sqrt{x \sin \theta_k + y \cos \theta_k} + r}{r_{3j}} \right) \end{array} \right)}{\sqrt{\left((x \cos \theta_k - y \sin \theta_k)^2 + (z + \frac{H}{2})^2 \right) \left(x^2 + y^2 - (x \sin \theta_k + y \cos \theta_k)^2 \right)}} \quad (\text{A39})$$

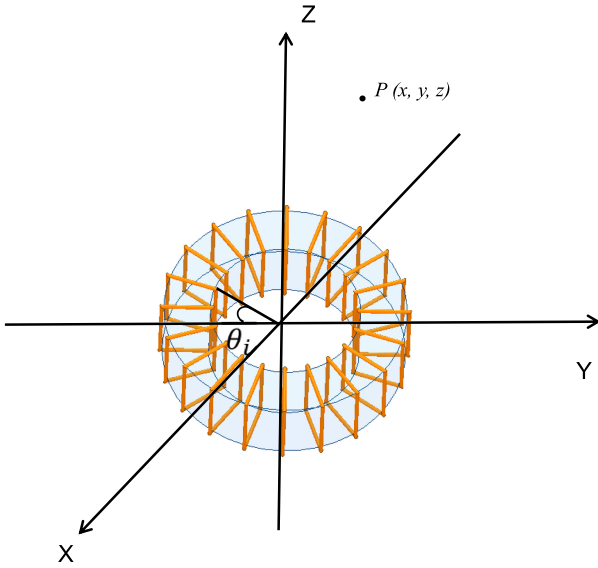


Fig. 32. Magnetic field flux density outside an inductor with 20 individual winding turns.

$$B_{y_{4\text{total}}} = \frac{\mu_0 I}{4\pi} \cdot \sum_{i=1}^N \frac{-x - r \sin \theta_i}{(x + r \sin \theta_i)^2 + (y + r \cos \theta_i)^2} \cdot \left(\frac{z + \frac{H}{2}}{r_{3i}} - \frac{z - \frac{H}{2}}{r_{4i}} \right) \quad (\text{A27})$$

$$B_{z_{4\text{total}}} = 0 \quad (\text{A28})$$

where

$$r_{1i} = \sqrt{(x + R \sin \theta_i)^2 + (y + R \cos \theta_i)^2 + \left(z - \frac{H}{2} \right)^2} \quad (\text{A29})$$

$$r_{2i} = \sqrt{(x + R \sin \theta_i)^2 + (y + R \cos \theta_i)^2 + \left(z + \frac{H}{2} \right)^2} \quad (\text{A30})$$

$$r_{3i} = \sqrt{(x + r \sin \theta_i)^2 + (y + r \cos \theta_i)^2 + \left(z + \frac{H}{2} \right)^2} \quad (\text{A31})$$

$$r_{4i} = \sqrt{(x + r \sin \theta_i)^2 + (y + r \cos \theta_i)^2 + \left(z - \frac{H}{2} \right)^2}. \quad (\text{A32})$$

The total magnetic flux density at point P is equal to the sum of all the individual winding turns, and it can be calculated as follows:

$$B_{x_{\text{total}}} = B_{x_{1\text{total}}} + B_{x_{2\text{total}}} + B_{x_{3\text{total}}} + B_{x_{4\text{total}}} \quad (\text{A33})$$

$$B_{y_{\text{total}}} = B_{y_{1\text{total}}} + B_{y_{2\text{total}}} + B_{y_{3\text{total}}} + B_{y_{4\text{total}}} \quad (\text{A34})$$

$$B_{z_{\text{total}}} = B_{z_{1\text{total}}} + B_{z_{2\text{total}}} + B_{z_{3\text{total}}} + B_{z_{4\text{total}}}. \quad (\text{A35})$$

Because the winding structure is symmetric, if a pair of symmetrically positioned current loops loop k and loop j have position angle θ_k and θ_j , where $\theta_j = \theta_k + 180^\circ$, based on triangular equations, (A36) and (A37) are satisfied

$$\sin \theta_k = -\sin \theta_j \quad (\text{A36})$$

$$\cos \theta_k = -\cos \theta_j. \quad (\text{A37})$$

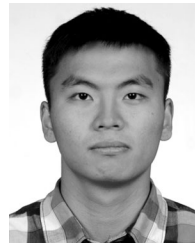
The magnetic flux density $B_{x_{1\text{total},k}}$ generated by loop k segment 1 at point P and flux density $B_{x_{1\text{total},k\&j}}$ at point P generated by both loop k and loop j can be expressed as follows (38) and (39) shown at the top of the this page.

As shown in (A38), due to the relationship given in (A36) and (A37), the value of (A39) is smaller than (A38) because of the subtraction between flux density of the two loops. If P is located at the middle of the inductor, which means $x = y = 0$, from (A29) and (A32), the distance between P and the four corners of the rectangular current loop is the same for loop k and loop j, which means in (A39), $r_{2k} = r_{2j}$, $r_{3k} = r_{3j}$, and (A39) becomes zero. Similar analysis can be applied to all other current segments. From (A33)–(A35), magnetic flux density generated by loop k and loop j at point P is zero in every direction.

For inductors with large number of turns evenly distributed on the core, the individual winding loops can be regarded as surface current on a toroid with the same direction. The surface current can be further divided into current strips and paired with symmetrical current segments at position angles satisfying the conditions (A36) and (A37). When point P is located at the center line of the inductor, full magnetic flux cancellation can be achieved. When point P is not located at the center line of the inductor, partial magnetic flux cancellation can be achieved, as shown in (A39). In general, the magnetic flux density outside the inductor due to winding turns is very small. The analysis agrees with Figs. 3(a) and 5(a).

REFERENCES

- [1] S. Wang, F. C. Lee, D. Y. Chen, and W. G. Odendaal, "Effects of parasitic parameters on EMI filter performance," *IEEE Trans. Power Electron.*, vol. 19, no. 3, pp. 869–877, May 2004.
- [2] S. Wang, R. Chen, F. C. Lee, and J. D. van Wyk, "Improved passive filter configurations for high-frequency conducted EMI in power electronics," in *Proc. Eur. Conf. Power Electron. Appl.*, Dresden, Germany, 2005, pp. 1–16.
- [3] S. Wang, F. C. Lee, W. G. Odendaal, and J. D. van Wyk, "Improvement of EMI filter performance with parasitic coupling cancellation," *IEEE Trans. Power Electron.*, vol. 20, no. 5, pp. 1221–1228, Sep. 2005.
- [4] S. Wang, R. Chen, J. D. Van Wyk, F. C. Lee, and W. G. Odendaal, "Developing parasitic cancellation technologies to improve EMI filter performance for switching mode power supplies," *IEEE Trans. Electromagn. Compat.*, vol. 47, no. 4, pp. 921–929, Nov. 2005.
- [5] S. Wang, F. C. Lee, and J. D. van Wyk, "Design of inductor winding capacitance cancellation for EMI suppression," *IEEE Trans. Power Electron.*, vol. 21, no. 6, pp. 1825–1832, Nov. 2006.
- [6] Y. Chu, S. Wang, N. Zhang, and D. Fu, "A common mode inductor with external magnetic field immunity, low-magnetic field emission, and high-differential mode inductance," *IEEE Trans. Power Electron.*, vol. 30, no. 12, pp. 6684–6694, Dec. 2015.
- [7] Y. Chu, S. Wang, J. Xu, and D. Fu, "EMI reduction with near field coupling suppression techniques for planar transformers and CM chokes in switching-mode power converters," in *Proc. IEEE Energy Convers. Congr. Expo.*, Denver, CO, USA, 2013, pp. 3679–3686.
- [8] C. Labarre and F. Costa, "Circuit analysis of an EMI filter for the prediction of its magnetic near-field emissions," *IEEE Trans. Electromagn. Compat.*, vol. 54, no. 2, pp. 290–298, Apr. 2012.
- [9] T. Q. Van Hoang, A. Bréard, and C. Vollaire, "Near magnetic field coupling prediction using equivalent spherical harmonic sources," *IEEE Trans. Electromagn. Compat.*, vol. 56, no. 6, pp. 1457–1465, Dec. 2014.
- [10] R. Wang, H. F. Blanchette, M. Mu, D. Boroyevich, and P. Mattavelli, "Influence of high-frequency near-field coupling between magnetic components on EMI filter design," *IEEE Trans. Power Electron.*, vol. 28, no. 10, pp. 4568–4579, Oct. 2013.
- [11] O. Aouine, C. Labarre, and F. Costa, "Measurement and modeling of the magnetic near field radiated by a buck chopper," *IEEE Trans. Electromagn. Compat.*, vol. 50, no. 2, pp. 445–449, May 2008.
- [12] L. Beghou, F. Costa, and L. Pichon, "Detection of electromagnetic radiations sources at the switching time scale using an inverse problem-based resolution method—Application to power electronic circuits," *IEEE Trans. Electromagn. Compat.*, vol. 57, no. 1, pp. 52–60, Feb. 2015.
- [13] A. Hariya *et al.*, "Circuit design techniques for reducing the effects of magnetic flux on GaN-HEMTs in 5-MHz 100-W high power-density LLC resonant DC–DC converters," *IEEE Trans. Power Electron.*, vol. 32, no. 8, pp. 5953–5963, Aug. 2017.
- [14] H. Yang and Z. Lu, "Analysis on near-field effect caused by stray magnetic field of integrated LLC transformer," in *Proc. Int. Power Electron. Appl. Conf. Expo.*, Shanghai, China, 2014, pp. 1349–1352.
- [15] T. Chen, "Inductor design for common-mode and differential mode inductors," M.S. dissertation, Dept. Elect. Comput. Eng., Univ. Texas at San Antonio, San Antonio, TX, USA, 2014.
- [16] R. Lai, Y. Maillet, F. Wang, S. Wang, R. Burgos, and D. Boroyevich, "An integrated EMI choke for differential-mode and common-mode noise suppression," *IEEE Trans. Power Electron.*, vol. 25, no. 3, pp. 539–544, Mar. 2010.
- [17] W. Tan, C. Cuellar, X. Margueron, and N. Idir, "A common-mode choke using toroid-EQ mixed structure," *IEEE Trans. Power Electron.*, vol. 28, no. 1, pp. 31–35, Jan. 2013.
- [18] M. Nave, "On modeling the common mode inductor," in *Proc. IEEE Trans. Electromagn. Compat.*, 1991, pp. 452–457.
- [19] S. Wang, F. C. Lee, and W. G. Odendaal, "Single layer iron powder core inductor model and its effect on boost PFC EMI noise," in *Proc. IEEE 34th Annu. Power Electron. Spec. Conf.*, 2003, vol. 2, pp. 847–852.
- [20] M. Misakian, "Equations for the magnetic field produced by one or more rectangular loops of wire in the same plane," *J. Res. Natl. Inst. Standards Technol.*, vol. 105, no. 4, pp. 557–564, Aug. 2000.
- [21] W. H. Hayt and J. A. Buck, *Engineering Electromagnetics*. New York, NY, USA: McGraw-Hill, 1981, vol. 6.
- [22] B. Zhang and S. Wang, "Analysis and reduction of the near magnetic field radiation from magnetic inductors," in *Proc. IEEE Appl. Power Electron. Conf. Exp.*, Tampa, FL, USA, 2017, pp. 2494–2501.
- [23] S. Wang, F. C. Lee, and W. G. Odendaal, "Characterization and parasitic extraction of EMI filters using scattering parameters," *IEEE Trans. Power Electron.*, vol. 20, no. 2, pp. 502–510, Mar. 2005.
- [24] S. Wang, F. C. Lee, and W. G. Odendaal, "Using scattering parameters to characterize EMI filters," in *Proc. IEEE 35th Annu. Power Electron. Spec. Conf.*, Aachen, Germany, 2004, vol. 1, pp. 297–303.



Boyi Zhang (S'17) received the B.S degree in electrical engineering from the Harbin Institute of Technology, Harbin, China, in 2015, and the M.S. degree in electrical and computer engineering from the University of Florida, Gainesville, FL, USA, in 2017. He is currently working toward the Ph.D. degree with Power Electronics and Electrical Power Research Lab, University of Florida.

He has authored and coauthored several IEEE conference and transaction papers. His research interests include electromagnetic interference, wide bandgap power device packaging, and magnetic components.

Mr. Zhang was the recipient of the Best Student Presentation Award in the Applied Power Electronics Conference in 2017 and 2019.



Shuo Wang (S'03–M'06–SM'07–F'19) received the Ph.D. degree in electrical engineering from Virginia Tech, Blacksburg, VA, USA, in 2005.

He is currently a Full Professor with the Department of Electrical and Computer Engineering, University of Florida, Gainesville, FL, USA. He has published more than 180 IEEE journal and conference papers and holds around 30 pending/issued US/international patents.

Dr. Wang was the recipient of the Best Transaction Paper Award from the IEEE Power Electronics Society in 2006, two William M. Portnoy Awards for the papers published in the IEEE Industry Applications Society in 2004 and 2012, respectively, and the prestigious National Science Foundation CAREER Award in 2012. He is an Associate Editor for the IEEE TRANSACTIONS ON INDUSTRY APPLICATIONS and a technical program Co-Chair for the IEEE 2014 International Electric Vehicle Conference.